Journal of Earth Science, *Vol. 34*, *No. 1*, *p. 101–121*, *February 2023* *ISSN 1674-487X*
Printed in China
https://doi.org/10.1007/s12583-020-1057-8

Analysis and Characterization of Pore System and Grain Sizes of Carbonate Rocks from Southern Lebanon

Mohamed K. Salah[*1], **Hammad Tariq Janjuhah**[1, 2], **Josep Sanjuan**[1, 3]
1. *Department of Geology*, *American University of Beirut*, *Riad El Solh*, *Beirut* 1107 2020, *Lebanon*
2. *Department of Geology*, *Shaheed Benazir Bhutto University*, *Sheringal KP* 10850, *Pakistan*
3. *Department of Earth and Ocean Dynamics*, *Faculty of Earth Sciences*, *University of Barcelona*, *Barcelona* 08028, *Spain*
Mohamed K. Salah: https://orcid.org/0000-0001-6079-6133; Hammad Tariq Janjuhah: https://orcid.org/0000-0002-1522-5988;
Josep Sanjuan: https://orcid.org/0000-0002-1275-6783

ABSTRACT: Carbonate rocks are common in many parts of the world, including the Eastern Mediterranean, where they host significant groundwater supplies and are widely used as building and ornamental stones. The porosity of carbonate rocks plays a critical role in fluid storage and retrieval. The pore structure connectivity, in particular, controls many properties of geological formations, as well as the relationships between the properties of individual minerals and the bulk properties of the rock. To study the relationships between porosity, rock properties, pore structure, pore size, and their impact on reservoir characteristics, 46 carbonate rock samples were collected from four stratigraphic sections exposed near Sidon, South Lebanon. The studied carbonate rocks are related to marine deposits of different ages (e.g., Upper Cretaceous, Eocene, and Upper Miocene). In order to understand the pore connectivity, the MICP (mercury injection capillary pressure) technique was conducted on ten representative samples. Results from the SEM analysis indicate the dominance of very fine and fine pore sizes, with various categories ranging in diameter from 0.1 to10 μm. The MICP data revealed that the pore throat radii vary widely from 0.001 to 1.4 μm, and that all samples are dominated by micropore throats. The grain size analysis indicated that the studied rocks have significant amounts of silt- and clay-size grains with respect to the coarser 'sand-size' particles, suggesting a high proportion of microporosity. Obtained results, such as the poorly-sorted nature of grains, high microporosity, and the high percentage of micropore throats, justify the observed low mean hydraulic radius, the high entry pressure, and the very low permeability of the studied samples. These results suggest that the carbonate rocks near Sidon (south of Lebanon) are possibly classified as non-reservoir facies.
KEY WORDS: petrophysics, mercury injection capillary pressure (MICP), micrite microtexture, microporosity, platform carbonates, southern Lebanon.

0 INTRODUCTION

Carbonate rocks are used as natural building stones, act as karst aquifers, and hydrocarbon reservoirs all over the world. Permeability, porosity, and other physical properties often show poor correlations in limestone. Many important reservoir parameters, such as capillary pressure (storativity), fluid flow, fluid accumulation and subsequent migration, and hydraulic conductivity, are influenced by the complicated carbonate microstructures (Gao et al., 2019; Müller-Huber et al., 2018; Schön, 2015; Mavko et al., 2009). Besides, the oil distribution in low/medium permeability reservoirs is largely controlled by the capillary pressure (Wang et al., 2018). These features distinguish carbonate reservoirs from sandstone reservoirs, which have more or less homogeneous pore space that is controlled essentially by particle properties such as shape, roundness, and sorting (e. g., Lima Neto et al., 2015; Anselmetti and Eberli, 1993).

Microporosity is a common type of porosity in carbonate rocks (e. g., Salah et al., 2020; Janjuhah et al., 2018; Lucia, 1995). Many of the supergiant oil fields of the Middle East occur in microporous limestones (Ehrenberg and Walderhaug, 2015; Soete et al., 2015; Burchette, 2012; Deville de Periere et al., 2011; Nurmi and Standen, 1997). These rocks are characterized by heterogeneous pore types, different pore sizes, complex pore geometry, and rock microtextures (e. g., Salah et al., 2020, 2018). The occurrence and distribution of microporosity are influenced by the crystallometry, morphology, and texture of the micrite particles (Janjuhah et al., 2019, 2018; Kaczmarek et al., 2015; Cantrell and Hagerty, 1999; Ahr, 1989; Moshier, 1989; Folk, 1959). In a low/medium-permeability reservoir, oil-gas imbibition and drainage are controlled mainly by micropores and occur mainly by the force of capillary pressure, which, thus, controls the hydrocarbon distribution in the

*Corresponding author: ms264@aub.edu.lb

Manuscript received January 24, 2020.
Manuscript accepted July 8, 2020.

Salah Mohamed K., Janjuhah Hammad Tariq, Sanjuan Josep, 2023. Analysis and Characterization of Pore System and Grain Sizes of Carbonate Rocks from Southern Lebanon. *Journal of Earth Science*, 34(1): 101–121. https://doi.org/10.1007/s12583-020-1057-8. http://en.earth-science.net

reservoir. The main factor affecting the capillary pressure is the pore structure of the rock (Shanley and Cluff, 2015; Al-Gharbi and Blunt, 2005), which explains why carbonate rocks of the same porosity and permeability might have different saturation properties (Wang et al., 2018).

Pore structure variations in carbonate rocks arise from the depositional setting, composition, sorting, granularity, and the different diagenetic processes (Hosseini et al., 2018; Baechle et al., 2004; Anselmetti and Eberli, 1999), and can add ambiguities to fluid behaviour in the rock. Compaction reduces, or even eliminates, original pores, while cementation produces a complicated pore structure. Dissolution results in more or less homogeneous secondary pores; dolomitization enhances the pore space of rocks, whereas recrystallization changes the pore size and geometry (Salah et al., 2016; Sun et al., 2015; Burchette, 2012; Anselmetti and Eberli, 1993). Moreover, tectonic deformation accompanied by uplift or subsidence is usually followed by denudation or deep burial, respectively, during which the rock pore structure can be completely reconstructed again (Wang et al., 2017; Hollis et al., 2010; Byrnes et al., 2009). In this way, evaluating the pore structure gives information not only on the hydrocarbon distribution but also on the understanding of the geological history of rocks.

There are many techniques for analyzing the pore structure of rocks, such as the mercury injection capillary pressure (MICP; e.g., Zhang et al., 2016; Xu and Torres-Verdín, 2013), nuclear magnetic resonance (NMR; Morriss et al., 1993; Dillinger and Esteban, 2014), multidimensional imaging techniques along with micro-CT and digital cores (Li et al., 2019; Lai et al., 2013; Al-Kharusi and Blunt, 2007), and model-based formulas such as the Kozeny-Carman equations (e.g., Theologou et al., 2015). The MICP method, in particular, is reliable, fast, convenient, and widely used to examine the pore size distribution, pore geometry, and pore throat sorting in reservoir rocks (e.g., Hosseini et al., 2018; Anovitz and Cole, 2015; Skalinski and Kenter, 2013; Rezaee et al., 2012; León y León, 1998; Wardlaw and McKellar, 1981; Wardlaw, 1976; Purcell, 1949). Mercury porosimetry applies to a wide range of pore sizes, starting from up to about 350 μm down to a few nanometers (e.g., Gao et al., 2019). Permeability—an important rock parameter characterizing the ease with which a rock permits the flow of fluids—is strongly correlated with MICP data (Swanson, 1981), and can be accurately estimated from capillary pressure measurements on sidewall plug samples and small cuttings (e.g., Nooruddin et al., 2014; Gao and Hu, 2013; Mao et al., 2013; Swanson, 1981 and references therein). Moreover, capillary pressure-related data is used by geologists, petrophysicists, and petroleum engineers to assess other reservoir parameters such as the reservoir quality index, pay versus non-pay, seal efficiency, fluid saturations, CO_2 sequestration, pore structure characteristics of coals, and the efficiency of recovery processes (Medina et al., 2018; Vavra et al., 1992).

The studied marine carbonate deposits are located in south Lebanon, about 6 km southeast of Sidon (Fig. 1). They comprise heterogeneous lithologies and different ages (Fig. 2), i.e., Upper Cretaceous chalky limestone (mudstone) strata at Choualiq, Eocene (Lutetian) limestones (wackestone) with chert bands from Qennarit and Upper Miocene marls, and sandy limestone (packstone/grainstone) beds from Maghdoucheh (Müller et al., 2010; BouDagher-Fadel and Clark, 2006; Dubertret, 1955). Detailed petrographical and petrophysical investigations of these carbonate rocks have not yet been completed; perhaps due partly to the current political instability and unfavourable logistics in southern Lebanon. Recently, Salah et al. (2020) studied the petrophysical properties of Mesozoic carbonate rocks in nearby areas in central and northern Lebanon. They found that these rocks are generally characterized by low to intermediate porosity, very low permeability, and high acoustic wave velocities. Moreover, even though some carbonate rocks have low porosity, they also have low acoustic wave velocities that clearly deviate from the well-established, inverse, porosity-velocity trends due mainly to the dominance of micro- and intercrystalline pores (Salah et al., 2020). Characterizing the pore sizes, pore types, and their shapes as well as their impacts on porosity, permeability, and fluid recovery in these carbonate deposits is crucial for rock identification and reservoir characterization. For this reason, the pore throat sizes of ten representative carbonate samples collected from southern Lebanon are analyzed by the MICP technique. Because the size distribution of particles controls many physical and chemical properties such as porosity, permeability, and wettability (Hu and Huang, 2016), a detailed laser particle size analysis (LPSA) on the ten representative samples was also conducted. We additionally measured the helium porosity and permeability of the rocks and petrographically investigated their facies and pore types by SEM and thin-section analyses. The obtained results are used to characterize the rock texture and pore throat size distributions to understand the observed petrophysical properties and reservoir characteristics.

1 GEOLOGICAL SETTING

Lebanon is featured by two mountain chains, Mount Lebanon in the west and the Anti-Lebanon in the east, both showing a general NNE-SSW trend. The two mountain chains are separated by the plain of the Bekaa syncline, which is filled mostly with Neogene non-marine deposits. The area of study is located at the south of Mount Lebanon near the coastal city of Sidon (Fig. 1). Its geology is represented mainly by marine carbonate rock successions of different ages affected by high tectonnism related to the Mesozoic/Paleogene Syrian Arc event and the Neogene Dead Sea transform fault system (Walley, 1998).

The oldest rocks exposed in the studied area are represented by the Upper Cretaceous Sannine Formation, often including younger Paleocene and Eocene deposits (Dubertret, 1955). The base of the formation consists of 200-m-thick white-gray monotonous marls and limestone beds rich in shells of planktonic foraminifera and calcareous nannoplankton. Based on the nannofossil content, Müller et al. (2010) identified several subdivisions within the Upper Cretaceous sequence of the Sannine Formation, i.e., Santonian, Campanian, and Maastrichtian. Dubertret (1945–1953) reported that these deposits grade upward to a 200-m-thick white marl interval with chert bands and nummulite-rich limestone. Based on the nummulite assemblage, Dubertret (1945 – 1953) dated the youngest Paleogene rocks exposed in the area as Middle Eocene (Lutetian). Müller

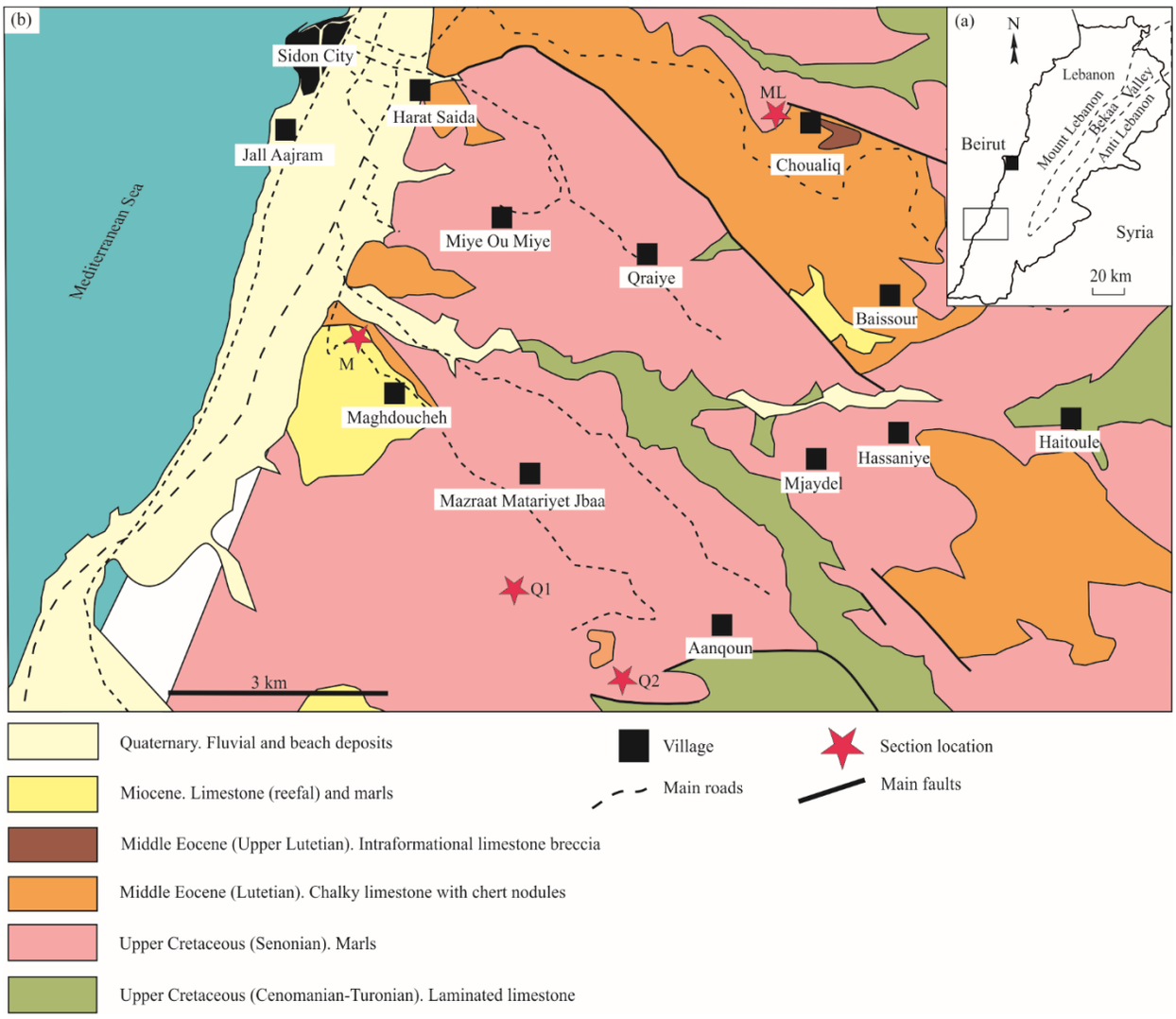

Figure 1. A geological map of the studied area in southern Lebanon (modified from Dubertret, 1945–1953). Red stars with capital letters represent the locations of the four stratigraphic sections (M. Maghdoucheh; Q1. Quennarit-1; Q2. Quennarit-2; and ML. Choualiq). The exposed rocks range in age from the Upper Cretaceous to the Quaternary. An inset to the top right (A) shows the study area outlined by the black rectangle.

et al. (2010) identified older deposits (Upper Danian to Upper Paleocene) near Sidon based on calcareous nannoplankton biostratigraphy (nannofossil Zone NP3-NP5). Younger Eocene deposits in the area are only exposed near the village of Choualiq, where an intraformational breccia outstands. In other areas of Lebanon, lateral equivalent deposits have been related to reefal Upper Lutetian facies (BouDagher-Fadel and Clark, 2006; Dubertret, 1955). However, near Sidon, these deposits are completely eroded, probably due to the tectonic uplift of the area and a consequent erosional period (Dubertret, 1955). This period of erosion occurred from the Late Eocene until the Late Oligocene, and it has been related to the second phase of the Syrian Arc deformation event (Müller et al., 2010; Walley, 1998). As a byproduct of the intense erosion, characteristic conglomerate intervals can be observed at the base of the Miocene marine deposits. These Miocene conglomerate sequences were mapped by Dubertret (1945–1953) near the villages of Maghdoucheh and Choualiq. Overlying carbonate sequences include 20-m-thick marly limestone and reefal limestone strata mainly located in the area of Maghdoucheh and Baissour, which lie upon older strata (Fig. 1). According to Müller et al. (2010), the oldest marine Miocene sediments in the area are Burdigalian in age (nannofossil Zone MN3-MN4). These authors also reported Langhian marine deposits in the area based on nannofossil biostratigraphy (nannofossil Zone MN5). These marine sequences were deposited in a deep environment (middle-outer shelf) within a shallowing upward trend (Müller et al., 2010). It has been related to the Middle Miocene (Langhian – Serravalian) marine transgression that postdates major uplift in the area, being largely post-orogenic (Walley, 1997; Dubertret, 1955). Müller et al. (2010) suggested that a tectonic event took place in the area during the Burdigalian due to the amount of reworked (older) nannofossil species within the Langhian deposits. The drop of the sea level during the Late Miocene, Pliocene, and Quaternary periods led to the erosion of the plateau and the deposition of fluvial terraces in the river valleys and beach deposits near the coast (BouDagher-Fadel and Clark, 2006; Dubertret, 1955).

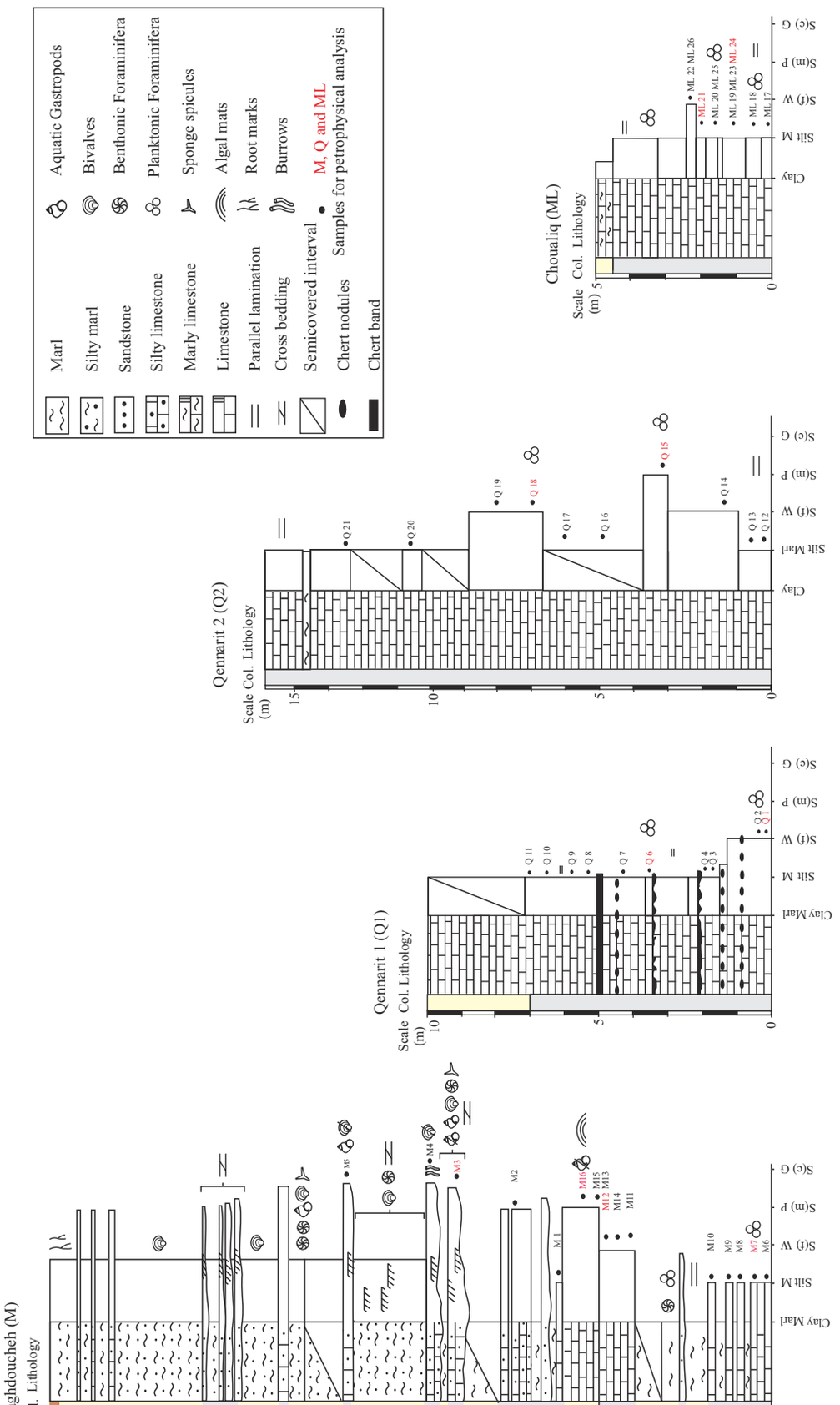

Figure 2. Stratigraphic logs of the four sections studied: Maghdoucheh, Qennarit-1, Qennarit-2, and Choualiq. The stratigraphic position of the samples extracted from the Maghdoucheh Section is represented by ML1 to ML16; the stratigraphic position of the samples extracted from the Qennarit sections is represented by Q1 to Q21; and the stratigraphic position of the samples extracted from the Choualiq Section is represented by ML17 to ML26.

2 DATA AND METHODS

In total, 46 specimens (at least one plug and a few small block samples from each site) were collected from four closely-spaced stratigraphic sections in southern Lebanon (Choualiq, Qennarit 1, Qennarit 2 and Maghdoucheh; Fig. 2). The exposed rocks are essentially marine carbonates of Upper Cretaceous, Eocene (Lutetian), and Upper Miocene ages. Sample selection was based on careful field investigation of outcrops. The Choualiq Section is composed of a 5-m-thick interval of monotonous light grey chalky limestone with mudstone textures (base of the section: 33º33'17"N, 35º26'2"E). Samples extracted from this section are referred to as 'Ml' in the text. The Qennarit Section-1 is located about 6 km southwest of the Choualiq Section on a road slope composed of 10-m-thick light grey limestone beds (mudstone/wackestone) alternated with black chert bands (base of the section: 33º30'8.2"N, 35º 24'10.6"E). The Qennarit Section-2 is located on a dirt road (base of the section: 33º29'29.3"N, 35º24'47.4"E) 1 km southeast of the first one. It is composed of 15 m of semi-covered grey limestone beds of wackstone/packstone facies rich in shells of planktonic foraminifera. Samples recovered from Qennarit sections are referred to as 'Q' in the text. The section of Maghdoucheh is situated on an anthropic cliff about 3 km south of Sidon, near the coastline (Fig. 1). It is composed of 20-m-thick grey and yellowish silty marls alternating with fossiliferous sandy limestones (packstone/grainstone) showing tractive structures such as cross-stratification and erosive bases (base of the section: 33º31'21.09"N, 35º22'48.8"E). Samples collected from this section are labelled as 'M' in the text.

Thin-sections and scanning electron microscopy (SEM) were performed on the tested rock samples to unravel their pore network and rock fabric. Ten representative thin-sections were prepared for petrographic analysis in the thin-section lab of the Department of Earth and Ocean Dynamics (Barcelona University, Spain). Thin-sections were impregnated with blue epoxy resin and later studied under both reflected and transmitted light microscopy at the Department of Geology and the Central Research Science Laboratory (CRSL) of the American University of Beirut. Later, these representative samples were analysed under the MIRA3 LMU SEM with an OXFORD EDX detector and TESCAN imaging. The SEM analysis allows comprehending the main diagenetic features, investigating the micropores in 3D, and assessing their impact on the petrophysical properties. Before the SEM analysis, each sample was cleaned with chloroform to remove any fluids and former acid effects. A standard procedure was followed to prepare a selected sample. A small rock portion was cut from the core plug and later placed on a metallic stub. Samples were later coated with gold using the SC-502 instrument for SEM observation to avoid conductivity. Three sets of images were taken for each sample at different magnifications (2 000, 5 000, and 10 000). In total, more than 150 microphotographs were taken for each studied sample. The software '*J. Microvision*' was used to measure the crystallometry of micrite particles in the quantitative analysis. The obtained SEM images indicate that the studied samples have significant amounts of fine carbonates (Fig. 3).

Routine core analysis provides important information on key rock parameters such as porosity, permeability, and fluid saturation. The more advanced analyses allow the investigation of pore size distribution, pore throat dimensions, fluid adsorption, and wettability (Wood and Hazra, 2017). The petrophysical, LPSA, and MICP measurements have been conducted on plugs extracted from the same samples used in the petrographic and SEM analyses. The drilled plugs were later sliced into lengths of 2–5 cm for subsequent measurements. The porosity-permeability (poro-perm) data were determined using the Core Laboratories measuring system (CMS-300™) at Houston, Texas, USA. This standard core-measuring system is an automated, computer-controlled unsteady state pressure decay permeameter and porosimeter that measures the core poro-perm-related parameters. The helium porosity (φ_{hel}) is estimated using the pore volume calculated at the designated confining stresses by the CMS-300™ and the sample grain volume obtained by an ultraporosimeter. This method has the advantage of compensating for the bulk volume compressibility due to the reduction in pore volume at overburden stress. Measuring gas permeability is corrected for the gas slippage effect to the Klinkenberg permeability (e. g., Jones, 1972). As described in Salah et al. (2020), the line obtained by plotting the obtained permeability versus the reciprocal mean pressures at five measurements is extrapolated to the vertical permeability axis to read the corresponding gas permeability. Grain density is calculated from the grain volume (determined after cleaning, drying, cooling, and weighing of the sample) and the sample weight.

The analysis of pore throat size distribution has been done by the MICP method (Marschall et al., 1995; Netto, 1993; Washburn, 1921). Selected samples were cleaned in a hot refluxing toluene to remove any fluids, and then with methanol to remove salts. Samples were then dried in an oven at 116 ºC prior to analysis. After drying, the plugs were placed in a desiccator containing silica gel for cooling. The clean and dry core samples were weighed and each placed in the bulb of a penetrometer so that the pore volume of the sample was approximately 25%–80% of the penetrometer stem. The sample and penetrometer were weighed together, then the penetrometer containing the sample was loaded into the low-pressure chamber of a Micromeritics Autopore-IV porosimeter. The penetrometer was evacuated to a pressure of less than 50 μm of mercury and then filled with mercury at a pressure of 0.5 psi. The bulk volume of the sample was determined at this point. Mercury is injected into the core pore system at incremental pressures from 0.5 to 30.0 psi. For a drainage cycle and the calculation of pore size distribution, the cumulative volume of mercury injected by incremental pressure changes up to a maximum of approximately 55 000 psi, with data being recorded at each pressure as described above. However, some researchers noticed that mercury does not occupy all of the available pore spaces in a specific sample, suggesting that the MICP results may be erroneously interpreted (e.g., Klaver et al., 2015). For this reason, the estimated pore volume through mercury injection is used to calculate the mercury injection porosity (φ_{mer}), which is then compared to the φ_{hel}. Other researchers adopted correction methods for the MICP data to account for the conformance errors and to better characterize the pore structure of tight shale rocks (e.g., Yu et al., 2019; Comisky et al., 2011; Sigal, 2009). Because of pore accessibility and conformance,

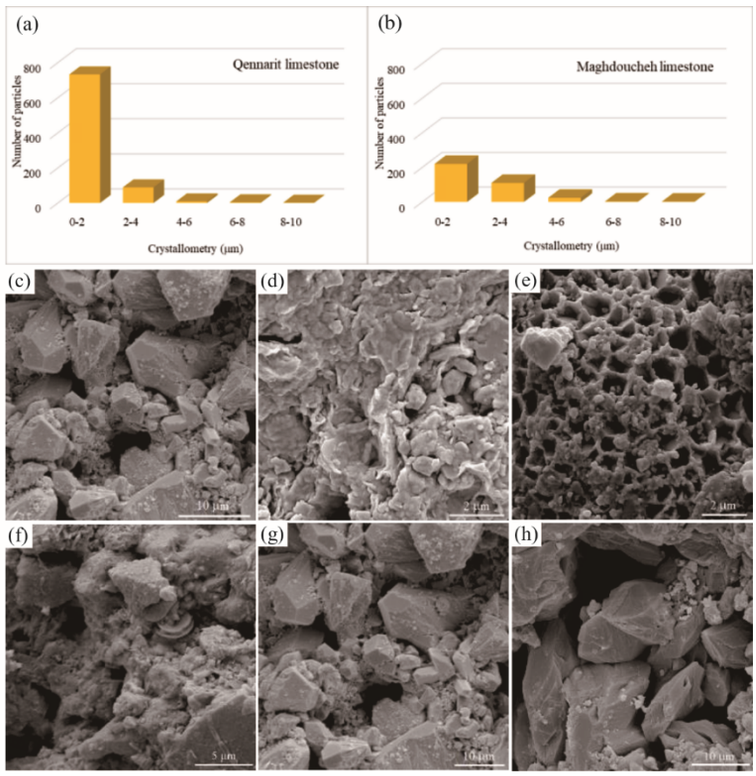

Figure 3. Histograms and SEM photomicrographs of the Upper Cretaceous, Eocene, and Miocene carbonate rocks exposed at Qennarit, Maghdoucheh, and Choualiq (southern Lebanon). (a) The crystallometry distribution of micrite particles in Qennarit carbonates; (b) the crystallometry distribution of micrite particles in the Maghdoucheh carbonates; (c) rounded, subrounded, trigonal, and rhombohedral-polyhedral particles resulting in a well-connected porous micrite (sample M12); (d) fitted bound-fitted fused anhedral micrite resulting in a tight micrite microtexture (sample Ml24); (e) very fine micropores representing the fitted fused anhedral texture of very fine isolated micropores with a pore diameter of 0.1–2 µm (sample Q6); (f) fine micropores characterizing a fitted bounding subhedral texture with little connectivity of isolated micropores from 2–4 µm in diameter (sample M 7); (g) medium micropores resulting in a subhedral texture. Note the micropores with poor to moderate connectivity and a pore diameter of 4–6 µm (sample M3); and (h) coarse micropores representing rhombic (micro-sub)-polyhedral microtexture with a pore diameter of 6–8 µm (sample M12).

MICP profiles obtained by Comisky et al. (2011) reveal a strong dependence on sample size. Their results verified the conformance correction approach proposed by Bailey (2009) to account for the pore volume reduction in the sample before mercury injection. Correction results obtained by Yu et al. (2019) showed that the simultaneous filling of interparticle voids with mercury impacts the pore volume in pore sizes greater than 1 µm. They additionally used the gas adsorption method to better measure very small pore sizes resulting from shale matrix compression and pore structure changes induced under the high injection pressure. The good agreement between the MICP-gas adsorption combined porosity and the helium porosity, as well as the similarly-computed pore sizes in the overlapped range, verify the correction method adopted by Yu et al. (2019) for shale rocks. In general, no consensus regarding a specific correction method has been achieved among researchers to this day. The studied rocks in Sidon (South Lebanon) are marine carbonates even though they contain "clay-size" fractions but not clay minerals, as explained later. Moreover, many authors (e.g., Labani et al., 2013; Liu et al., 2014) have proposed that the MICP method can provide proper pore size information in the range of 3.6 nm and 100 µm, which approximately encompasses the range detected in our representative samples (2 nm to 1.5 µm). However, the excellent fit between the φ_{hel} and the φ_{mer} (Fig. 4a), as well as the positive relationships between flow properties and pore throat sizes (later sections), confirm the efficiency of the injection method to characterize the pore throat sizes of the tested samples. It should also be noted that before mercury injection data can be applied to the reservoir, data must be converted using simple conversion formulae from the laboratory air/mercury system to the reservoir brine/hydrocarbon system in the subsurface (Vavra et al., 1992). The applied mercury pressure (psi) and pore throat radii (in µm) are routinely plotted versus mercury saturation fraction. The resulting curves are dependent on the pore size distribution, rock tightness, rock type, and saturation history (i.e., mercury intrusion versus fluid extrusion). Thus, the path of the drainage curve reflects the petrophysical characteristics of the tested sample. The shape of the mercury intrusion curves (i.e., flat vs steep) and their position on the vertical pressure scale, in conjunction with data on other measured petrophysical properties, shed light on the connectivity of pore structures and the potential of the tested rock to conduct fluids (Medina et al., 2018).

Injected cumulative volumes of mercury are expressed as a fraction of the total pore volume of the sample. The minimum radius 'r' of the pore throat (in µm) which can be penetrated by mercury at a given pressure (e.g., Washburn, 1921) is given by the Young-Laplace equation as

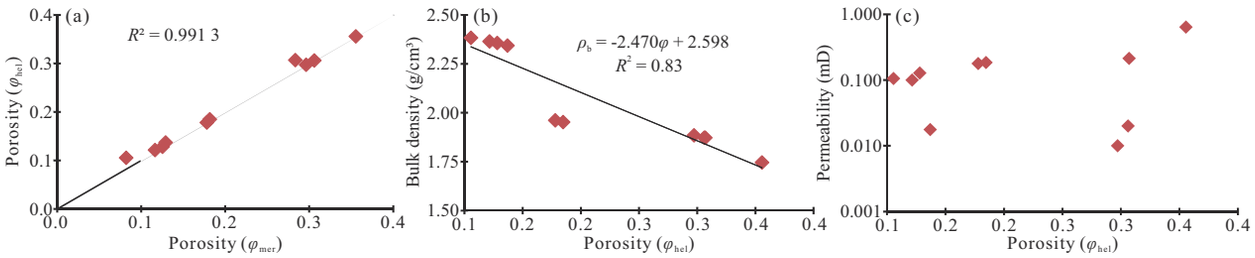

Figure 4. Crossplots between the measured helium and mercury porosities (φ_{hel} vs φ_{mer}) (a), porosity vs bulk density (b), and porosity vs permeability (c).

$$r = 2\sigma \cdot \cos\theta \cdot C/Pc \quad (1)$$

where σ is the interfacial tension between air and mercury (485 dynes/cm); θ is the contact angle between air and mercury (140º, e. g., Schlömer and Krooss, 1997); Pc is the capillary pressure; and C is a conversion constant which is equal to 0.145 038 (e. g., Adamson and Gast, 1997). With the data derived from this equation, we can construct a drainage curve between the applied pressure and the fraction of mercury saturation and another graph between the fraction of injected pore volume (v) and the pore throat radius (r). The differential of this equation gives the pore throat size distribution (PSD) function.

$$\mathrm{PSD} = \mathrm{d}v/\mathrm{d}\log r \quad (2)$$

which is smoothed using 1-2-1 smoothing: $\mathrm{PSD}_i = (\mathrm{PSD}_{i\text{-}1} + 2\mathrm{PSD}_i + \mathrm{PSD}_{i+1})/4$; and finally normalized: $\mathrm{PSD}_{\mathrm{normal}\,i} = \mathrm{PSD}_i/\mathrm{PSD}_{\mathrm{max}}$ (e. g., Hosseini et al., 2018). The normalized PSD function can be used to identify pore throat size groupings and the relative proportions of pore volume represented by macro-pore throats (>1.5 μm), meso-pore throats (1.5 to 0.5 μm), and micro-pore throats (<0.5 μm), referred to in the text as macroports, mesoports, and microports, respectively. The PSD function is also related to the material permeability and can thus be used to predict the permeability of the investigated sample (Schmitt et al., 2013).

The mean hydraulic radius (MHR) is the average pore throat size of the sample as determined by the MICP technique. The Swanson's parameter (Swanson, 1981) relates the capillary pressure to permeability (Hosseini et al., 2018). This parameter is determined first by calculating Sb/Pc (where Sb is mercury saturation, % bulk volume) at all pressures for a sample, then taking the highest of these values.

Adapted from Purcell (1949), the theoretical cumulative permeability, Kt_i of a sample with a given pore size distribution, (r_0 to r_i), can be expressed as

$$Kt_i = \sum_{i=0}^{n} ri^2 \cdot \Delta_{Si} \quad (3)$$

which can be normalized such that the maximum value is 1.0. A cumulative permeability distribution function (PDF) is given by the following equation.

$$\mathrm{PDF}_{\mathrm{normal}\,i} = Kt_i/Kt_{\mathrm{max}} \quad (4)$$

The flow zone indicator (FZI) is used to categorize the layers of rock into hydraulic units having identical production properties and is related to permeability and porosity by the following relation.

$$\mathrm{FZI} = \frac{0.031\,4\sqrt{\left[\frac{K}{\varnothing}\right]}}{\left[\frac{\varnothing}{1-\varnothing}\right]} \quad (5)$$

Different depositional settings and lithology with subsequent diagenetic processes control the pore structure of the reservoir and, therefore, affect the FZI data (Nabawy et al., 2018). The obtained results of porosity, permeability, and a summary of the MICP data as well as the related parameters are listed in Table 1.

Studies of grain size distribution in carbonate rocks provide information on the depositional processes and the seabottom currents (e. g., Michels, 2000; Rea and Hovan, 1995). They are also useful in oceanic studies for characterizing climatic fluctuations and changes in the sediment provenance (Trentesaux et al., 2001). Therefore, the laser particle size analysis (LPSA) was performed to measure the particle size distribution and the average grain size. The analyzed representative samples are moderately well-cemented with a wide range of grain sizes (from 1.68 mm to clay-sized). To obtain an accurate LPSA, correct disaggregation of the samples is required while extreme care is taken to un-break the grains. The samples were added to a solution of 5% sodium hexa-metaphosphate before measurement to de-ionize particles. The obtained LPSA data is given in Table 2.

The 'volume of shale (V_{sh})' is calculated from the proportions of fine components that range from 'clay-sizes' through to medium-grained 'silt sizes'. The standard deviation indicates the span of the measured particle size distribution. The specific surface area (SSA) of a sample is an indicator of the total surface area of the grains constituting the rock. It is an important property of reservoir rocks and in petroleum engineering as it characterizes the surface area of a rock exposed to fluids, and affects the magnitude of adsorption of the particles of a rock to the fluids passing through the rock pores. It also describes the average size and the degree of dispersion of rock particles (Hu and Huang, 2016). It is calculated as the total surface area of the matrix (which is the same as the total internal surface area of the void space) divided by the total volume of the rock and thus can be expressed as $\mathrm{cm^2/cm^3}$ ($\mathrm{cm^{-1}}$) or $\mathrm{m^2/cm^3}$. It increases with the decrease in grain size; therefore, it is expected to be positively correlated to the volume of clay- and silt-size components of sedimentary rocks.

Table 1 Summary of the petrophysical and MICP test results.

Sample	P_{th} (psi)	MHR (μm)	Median (μm)	φ_{mer}	φ_{hel}	Mesoports (%)	Microports (%)	K (mD)	ρ_g (g/cm^3)	ρ_b (g/cm^3)	Swanson parameter (10^{-3})	FZI (μm)
M3	79	0.241	0.165	0.355	0.356	10	90	0.640	2.69	1.75	29	0.09
M7	1 382	0.018	0.026	0.125	0.128	0	100	<0.01	2.70	2.36	1.83	--
M12	90	0.274	0.156	0.116	0.122	17	83	0.104	2.70	2.37	10.4	0.28
M16	2 081	0.011	0.013	0.082	0.106	0	100	<0.01	2.65	2.38	0.478	--
Ml21	9 334	0.002	0.003	0.178	0.178	0	100	<0.01	2.30	1.96	0.338	--
Ml24	8 143	0.002	0.003	0.182	0.185	0	100	<0.01	2.31	1.95	0.329	--
Q1	1 816	0.016	0.025	0.296	0.297	0	100	0.01	2.61	1.89	3.49	0.03
Q6	1 816	0.019	0.033	0.306	0.306	0	100	0.02	2.61	1.87	4.78	0.03
Q15	235	0.138	0.241	0.283	0.307	0	100	0.21	2.71	1.87	33.7	0.08
Q18	405	0.085	0.153	0.129	0.137	0	100	0.02	2.71	2.34	9.68	0.11

P_{th} = mercury entry pressure; MHR = mean hydraulic radius; φ_{mer} = mercury porosity; φ_{hel} = helium porosity; mesoports = proportion of mesopore throats; microports = proportion of micropore throats; K = permeability; ρ_g and ρ_b =grain and bulk densities; FZI = flow zone indicator (see text for more details).

3 RESULTS

3.1 SEM Analysis

3.1.1 Crystallometry of micrite particles

The crystallometry classes are based on the measurement of the maximum length of the micrite particles from an SEM photomicrograph (Janjuhah et al., 2018). Based on this classification, five types of micrite particles with sizes of <10 mm are observed in the studied samples. These classes can be described as very fine (0.1–2 mm), fine (2–4 mm), medium (4–6 mm), coarse (6–8 mm) and very coarse (8–10 mm) (Figs. 3a–3b). The size of the micrite particles varies from one locality to another. The rocks of both Qennarit (Fig. 3a) and Maghdoucheh (Fig. 3b) are composed dominantly of very fine to fine micrite particles, although with a higher proportion of the very fine micrite in the Qennarit samples. Low proportions of coarse and very coarse micrites are also detected in the samples of both localities (Fig. 3).

3.1.2 Micrite microtexture

The micrite microtexture of representative samples has also been investigated by SEM analysis. Based on the classification of Janjuhah et al. (2018), the micrite microtexture of the studied samples can be subdivided into two groups (Figs. 3c–3d), i.e., well-connected inter-crystalline and tight micrite microtextures. The well-connected micrite microtexture consists of rounded, subrounded, trigonal, and rhombic-to-polyhedral micrite grains (Fig. 3c) and is observed in sample M12 from Maghdoucheh carbonates. The second group consists of tight micrites of fitted, bound, subhedral to fitted fused anhedral micrites (Fig. 3d), detected in sample Ml24 from Choualiq.

3.1.3 Microporosity

Based on the classification of Janjuhah et al. (2018), which covers a wide range of crystallometry, morphology, texture, and depositional setting, four classes of microporosity are observed in the studied rocks from southern Lebanon. These classes are based on the size of the micropores present in each sample and comprise very fine micropores (0.01 – 2 mm), fine micropores (2 – 4 mm), medium micropores (4 – 6 mm), and coarse micropores (6–8 mm), respectively (Figs. 3e–3h). Based on the SEM images, among the four classes of microporosity, class-1 (very fine micropores), and class-2 (fine micropores) represent 70% of the observed microporosity. The very fine micropores are mainly observed in the chalky and fine limestone facies (mudstone/wackestone) of the Choualiq and Qennarit samples with fitted fused anhedral micrite particles. On certain occasions, it is also observed in fitted bounded subhedral textures. For example, very fine to fine micropores are detected in samples Q6 and Ml24 (Figs. 3d and 3e). These very fine micropores are isolated in nature with narrow pore throats. The very fine class of micropores is commonly observed in the top part of Maghdoucheh and Qennarit Section-2 rocks (Fig. 2). Fine micropores are commonly present in the lower part of Maghdoucheh and Qennarit Section-1 (Fig. 2), with dominant moldic, intraparticle, and vuggy pores. These micropores are mostly observed in subhedral, rhombic (micro-sub)-polyhedral, fitted bounding subhedral, and fitted fused anhedral textures. The micropores are also isolated in nature when observed as fitted

Table 2 Results of the particle size analysis (LPSA)

S. No.	Sand-size (%)					Silt-size (%)				Clay-size (%)	V_{sh} (%)	SSA (m^2/cm^3)	Mean (μm)	Md. (μm)	Std. Dev. (mm)	Srt., (mm)	Skw. (mm)	Kurt. (mm)
	VCRS	CRS	MED	FIN	VFIN	CRS	MED	FIN	VFIN									
M3	0.0	0.0	0.0	0.5	11.4	18.0	18.0	17.6	16.9	17.8	70	1.00	21.3	14.5	0.025	2.655	0.945	0.248
M7	0.0	0.0	0.0	0.5	7.4	11.2	15.0	20.5	22.1	23.3	81	1.24	13.6	9.0	0.017	2.365	1.165	0.181
M12	0.4	8.3	12.3	8.0	12.2	14.5	13.8	12.9	9.4	8.1	44	0.55	95.6	41.4	0.166	3.902	1.235	0.181
M16	0.0	0.0	0.7	7.1	16.5	16.3	13.4	13.4	14.6	17.9	59	0.94	33.0	19.8	0.041	3.338	0.846	0.251
Ml21	0.0	0.0	0.0	5.0	17.9	21.0	16.8	13.3	12.5	13.5	56	0.78	32.9	24.7	0.037	2.816	0.709	0.267
Ml24	0.0	0.0	0.0	2.6	12.5	19.1	19.1	15.9	15.0	15.8	66	0.89	24.5	18.3	0.028	2.685	0.771	0.245
Q1	0.0	0.0	0.0	1.0	4.0	7.7	10.2	17.3	27.4	32.3	87	1.55	8.7	6.0	0.011	2.080	1.279	0.147
Q6	0.0	0.0	0.0	0.0	1.1	2.9	6.1	19.4	33.0	37.5	96	1.78	5.9	5.0	0.005	1.720	1.042	0.204
Q15	0.0	0.0	0.0	0.4	4.1	12.7	19.1	18.9	17.9	26.7	83	1.35	13.5	9.6	0.015	2.522	0.931	0.236
Q18	0.0	0.0	0.1	2.8	9.3	15.7	18.1	17.7	16.3	20.0	72	1.09	19.9	13.3	0.024	2.682	0.958	0.220

VCRS. very coarse; CRS. coarse; MED. medium; FIN. fine; VFIN. very fine; V_{sh}. total volume of clay-size up to medium silt-size components; SSA. specific surface area; Mean. mean grain size; Md. median grain size; Std. Dev. standard deviation; Srt. sorting; Skw. skewness; Kurt. kurtosis (refer to the text for more details).

bounding subhedral and fitted fused anhedral textures. This class of fine micropores has minor interconnections and thus less impact on enhancing permeability.

3.2 Petrophysical Properties

Petrophysical properties obtained from lab analyses are listed in Table 1. The ρ_b and ρ_g vary from 1.75 to 2.38 g/cm^3 and from 2.3 to 2.71 g/cm^3, respectively. The measured φ_{hel} varies from 0.106 to 0.356, with an average of 0.212. On the other hand, the φ_{mer} varies from 0.082 to 0.355, with a close average of 0.205. The perfect correlation between the two porosities (with $R^2 > 0.99$) reflects the consistency between the two differently measured porosities (Fig. 4a). The measured porosity is inversely related to the bulk density (Fig. 4b). Samples Ml21 and Ml24 have a lower bulk density relative to their porosities of 0.18 and 0.19. The permeability of the tested samples is generally very low (<1 mD). Although samples Q1 and Q6 have high porosities of 0.30 and 0.31, their permeability is very low (Table 1), possibly due to a large proportion of fine micropores. The poro-perm relationship (Fig. 4c) indicates, however, that the permeability values of six samples are positively correlated with φ_{hel}. The M12 sample deviates slightly from the observed trend and has a relatively higher permeability given its porosity of 0.12. The petrographic study and the SEM analysis also confirm that depositional texture and diagenetic processes (such as micritization, cementation, and dissolution) played a role in the destruction of porosity and increasing the percentage of microporosity at the three studied localities (Figs. 5a–5j); hence the low permeability. The petrographic analysis of Maghdoucheh samples indicates a grainier texture with dominantly moldic and intraparticle porosity (Fig. 5h). However, at Qennarit and Choualiq, the textures are muddier with abundant matrix and the proportion of micropores is high (as also documented previously by the presence of very fine and fine micropores), resulting in high microporosity but without any impact on permeability (Figs. 5a, 5b, 5d–5e). The permeability reduction in the current samples is not limited to the microporous textures but also to the cement and matrix (Fig. 5e). The secondary porosity in Maghdoucheh and Qennarit localities, developed after dissolution, comprises moldic and vuggy porosities. These types of observed pores are mostly isolated in nature, justifying the detected moderate/high porosity but low permeability.

The computed FZI values of six samples using the obtained poro-perm data have an average of only 0.1 and vary from 0.03 to 0.28 μm, which characterize the investigated rocks as non-reservoir facies of very low permeability (Nabawy and Barakat, 2017).

3.3 MICP Data and Related Parameters

The applied mercury pressure (psi) and pore throat radii (μm) are plotted versus mercury saturation fraction in Figs. 6a and 6b. Although the applied pressure started at 0.5 psi, a minimum pressure of 79 psi was necessary to inject mercury into the samples' pore space (sample M3). Some samples (Ml21 and Ml24) did require much higher threshold pressures of 9 334 and 8 143 psi, respectively, for mercury injection (Table 1, Fig. 6a). Full mercury saturation (i.e., 100%) has been achieved for all samples at a pressure of 55 000 psi, confirming the ability of the injection scheme to investigate the pore structure information of the presently-studied low-permeability rocks (e.g., Gao et al., 2019).

Mercury pressures of less than 1 000 psi were enough to fill ~60% of the pore volume with mercury for four samples: M3, M12, Q15, and Q18; whereas it was necessary to apply pressures of up to 10 000 psi to reach the same saturation for samples M7, M16, Q1, and Q6. Samples Ml21 and Ml24 required even much higher pressures to inject mercury into their micropores.

Although they are all carbonate rocks, it is clear that the investigated representative samples have heterogeneous crystal sizes (Figs. 3a–3b). Pore throat radii vary widely in the tested samples, from 0.002 to 1.4 μm. No macroports (i.e., >1.5 μm) have been detected in the studied samples. The greatest pore throat radii are detected in samples M3 and M12 (Fig. 6b), which could be related to the presence of medium to coarse mi-

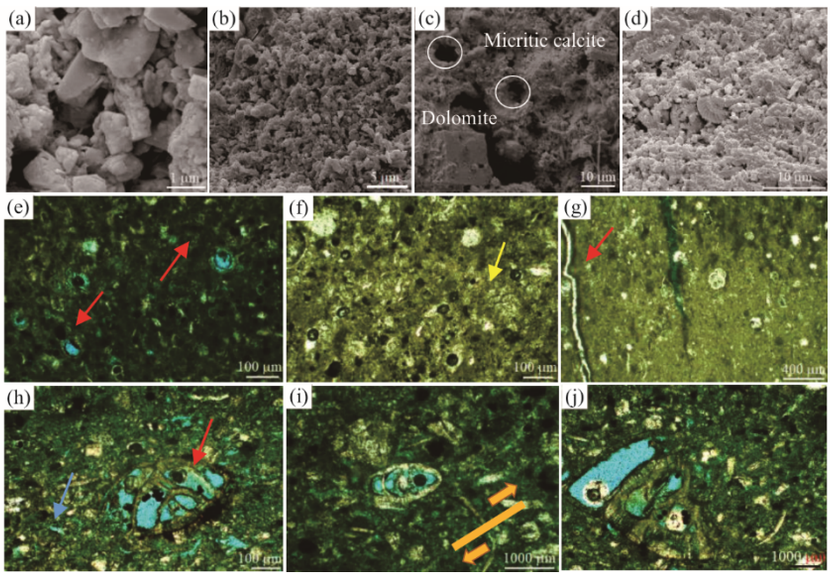

Figure 5. SEM and thin-section photomicrographs of the studied carbonate rocks. (a) Very fine micropores in sample Q18; (b) very fine to fine micropores in sample Ml21; (c) disordered dolomite representing micritized forams (white circles) with a calcite-dominated cement filling the pore spaces (sample M3); (d) very fine to fine micrite microtexture with a fossil of *coccolith* (sample Q15); (e) highly micritized skeletal components (red arrows) with abundant cement and matrix (sample Q15); (f) calcite cementation (yellow arrow) (sample M7); (g) neomorphism; the fracture and the filling of the veins post-dated an early diagenetic process (red arrow) (sample Q1); (h) fabric-selective dissolution (first stage of dissolution), with the red arrow indicating the intraparticle porosity while the blue arrow indicates the moldic porosity. The moldic porosity is partially filled with late calcite cement (sample M3); (i) collapsed and fractured micrite envelops (arrows) and fractured bioclasts with the partial dissolution of the shell and neomorphism (sample M3); and (j) fabric-selective dissolution (sample M3).

cropores of different sizes ranging from 4–8 μm (Figs. 3g–3h). The petrographic analysis of sample M3 also indicates that the sample is characterized by a high fabric-selective dissolution (Figs. 5h–5j).

Samples M3 and M12 are the only rocks with low percentages of mesoports (10% and 17%, respectively). The remaining pore throats of these two samples, as well as all the other samples, are microports (i.e., <0.5 μm). This explains the notably very low permeability of the studied rocks. In particular, samples Ml21 and Ml24 are dominated by very small micropores (<0.01 μm), very low permeability, and are thus intruded at high mercury entry pressures (Fig. 6a).

The median pore throat radii (the pore throat radius equivalent to 50% mercury saturation) of the selected samples are listed in Table 1, and are presented in Fig. 6b by the dashed horizontal line. The median pore throat radii varied from 0.003 to 0.241 μm with an average of 0.082 μm. These small values are consistent with the dominance of microports and the small proportion of mesoports in only two samples. Samples Ml21 and Ml24 have, again, the lowest median pore throat radii of 0.003 μm, whereas sample Q15 has the highest median of 0.241 μm (Fig. 6b). The permeabilities of the first two samples are <0.01 mD, but they are 0.21 mD for sample Q15. The median pore throat radii in eight out of the tested samples are larger than the MHR, indicating the dominance of microports, whereas samples M3 and M12 have greater MHR because of the presence of some mesoports (Table 1). In particular, samples M7, M16, M21, M24, Q1, and Q6 have very small median pore throat sizes that vary from 0.003 to 0.033 μm confirming the abundance of microports in these samples.

3.4 LPSA Results

The obtained grain size parameters are given in Table 2, while the distributions of size fractions for five representative samples are shown in cumulative and frequency histograms (Fig. 7). Grain sizes vary widely over 3 orders of magnitude, from 0.001 to 1 mm. The mean grain sizes vary widely between 6 and 96 μm, with a small average of 27 μm (Table 2). On the other hand, median grain sizes vary from 5.0 to 41.4 μm (average 16.2 μm). Values of the standard deviation vary largely from 0.005 to 0.166 mm (average 0.037 mm) implying moderate or poor grain sorting. The skewness values vary from 1.28 to 0.71 mm (average 1.0 mm), indicating that the studied samples are fine-to-medium skewed. Sample M12 contains a high 'sand-size' percentage of 41.2% (Fig. 7), and thus has the largest mean grain size (Table 2).

Samples M7, Ml24, Q1, Q6, Q15, and Q18 are dominated by "silt-" and "clay-size" particles; thus, they have the lowest mean grain sizes (Table 2). Most of these samples also exhibit steeply rising cumulative curves at the fine component portions (Fig. 7).

The SSA of the tested samples varies from 0.55 to 1.78 m^2/cm^3 (average 1.12 m^2/cm^3). It is negatively correlated with the sand-size percentage but positively correlated with the fine 'silt-' and 'clay-size' amounts, which correspond to the V_{sh} in clastic rocks (Figs. 8a–8b). It is also negatively correlated with the mean particle size (Fig. 8c).

4 DISCUSSION

4.1 Petrophysical Characteristics and Microstructures

Data presented in Table 1 shows that only two samples (M16 and Q15) have slightly higher φ_{hel} than φ_{mer}, which might

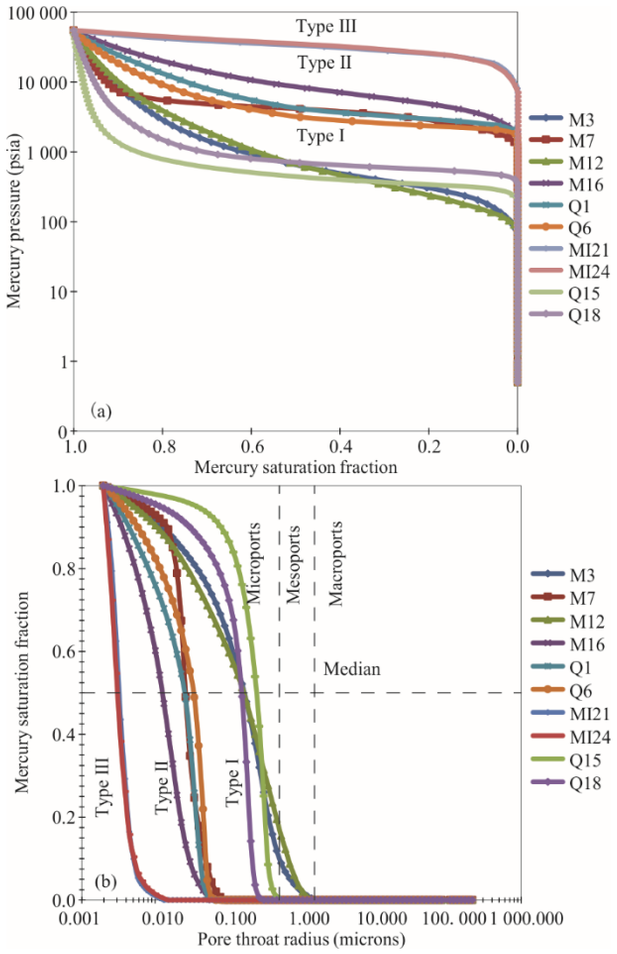

Figure 6. Normalized mercury injection capillary pressure intrusion curves: the fraction of mercury saturation vs the applied pressure (a), and vs the pore throat size distribution (b).

be related to the different viscosity of the two fluids used to measure porosity (Medina et al., 2017). Although not the highest, the shale-size fraction of the two samples is 59% and 83%, respectively. Samples Q1 and Q6 have the highest shale-size fraction as 87% and 96% (Table 2), and thus very low permeability (≤0.02 mD). These samples contain high amounts of very fine and isolated micropores (Fig. 3e). Although samples M7 and M16 have moderate porosities (0.13 and 0.11, respectively), their permeabilities are also very low (<0.01 mD) perhaps due to higher percentages of fine components (Table 2; Fig. 3f). Sample M12 possesses the highest sand-size and the lowest clay-size components as well as the lowest V_{sh}; hence, a relatively higher permeability of 0.10 mD at the measured porosity. This sample also has a significant proportion of mesoports (17%), a low P_{th}, and the highest MHR (Table 1 and Fig. 6). However, this sample has a moderate porosity (0.12) and a very low permeability of 0.1 mD. The six samples with permeabilities ≥0.01 mD display a general direct poro-perm relationship, although with some scatter (Fig. 4c). Because carbonate rocks have originally complex primary fabrics, various proportions of fine components, and are prone to prolonged diagenetic alterations (e. g., compaction, cementation, dissolution, precipitation, dolomitization, etc.), they usually exhibit very complicated poro-perm relationships (Lapponi et al., 2011; Dewit et al., 2012). Samples Q1 and Q6 have very low permeabilities of 0.01 and 0.02 mD, respectively, although their porosities are high (~0.3). These two samples have a large proportion of micropores (Figs. 3e and 5g) and the highest shale-size fraction (Table 2). Variations in bulk density are mainly related to porosity variations (e. g., Salah et al., 2016, 2019). Two samples (MI21 and MI24) deviate from the linear relationship between porosity and bulk density (Fig. 4b), where they may have either lower porosity at the given bulk density, lower bulk density at the given porosity, or both low porosity and density. The small MHR and high P_{th} (Table 1; Fig. 6a), suggest that these two samples have higher proportions of micro- and isolated pores (Fig. 5b) that significantly reduce their measured porosity. As revealed by their low grain densities of 2.3 and 2.31 g/cm^3 (Table 1), these two samples might also have larger proportions of light minerals that reduce their bulk density. The observed variations in grain density are relatively large and might be induced by alterations in the rock fabric from the dense sparite to the finer micritic fabrics (Pentecost, 2005).

Samples M16 and MI21 contain 24% and 23% sand-size grains, respectively, but different porosities (0.11 and 0.18), very low permeabilities, moderate P_{th}, and small MHR. Samples M3 and MI21, on the other hand, have close clay-size fractions of 17.8% and 13.5%, respectively. However, sample M3 has the highest porosity compared to the moderate porosity of sample MI21 (Table 1). The high porosity of sample M3 (0.36) can be justified on the basis of its packstone/grainstone texture (Fig. 3g). Moreover, carbonate grains are mainly bioclasts (large fragments of mollusks, echinoids, and empty chambered benthic foraminifera) and micritic pellets. Samples Q1 and Q6 contain significant clay-size fractions of 32.3% and 37.5%, respectively (Table 2); hence, very high porosity (micro), but very low permeability (Table 1). The abundance of lime-mud may be related to contamination from underlying and overlying partially-covered marly intervals (Fig. 2). The relative abundance of lime-mud in sample MI21 is related to the facies type encountered in the Choualiq Section as a chalky/muddy limestone (Fig. 2). The samples that are dominated by silt- and clay-size particles (M7, MI24, Q1, Q6, Q15, and Q18), have low MHR, very low permeability, moderate/high entry pressures even though some of them have high porosities (Table 1). Petrographic and SEM images also support the variations in the measured grain sizes (Figs. 5a and 5h). The moderate porosity developed during the deepening of the platform was accompanied by enrichment with fine components since the Maghdoucheh carbonates are grain-supported, but the Qennarit and Choualiq samples are muddy in terms of depositional textures (Fig. 5a). However, based on the crystallometry of the micrite particles, very fine micrites are dominant in both localities (e.g., Maghdoucheh and Qennarit) with dominant very fine micropores, which could be the reason why the pores are isolated and have no positive impact on permeability (Figs. 3a–3b, and Fig. 5e). The SEM image of sample MI24 points to a low number of but heterogeneous pores (Fig. 3d). Although sample MI21 has densely-developed and uniformly-distributed interconnected pores (Fig. 5b), they are very small in size as revealed by their MICP-derived parameters (Table 1). On the oth-

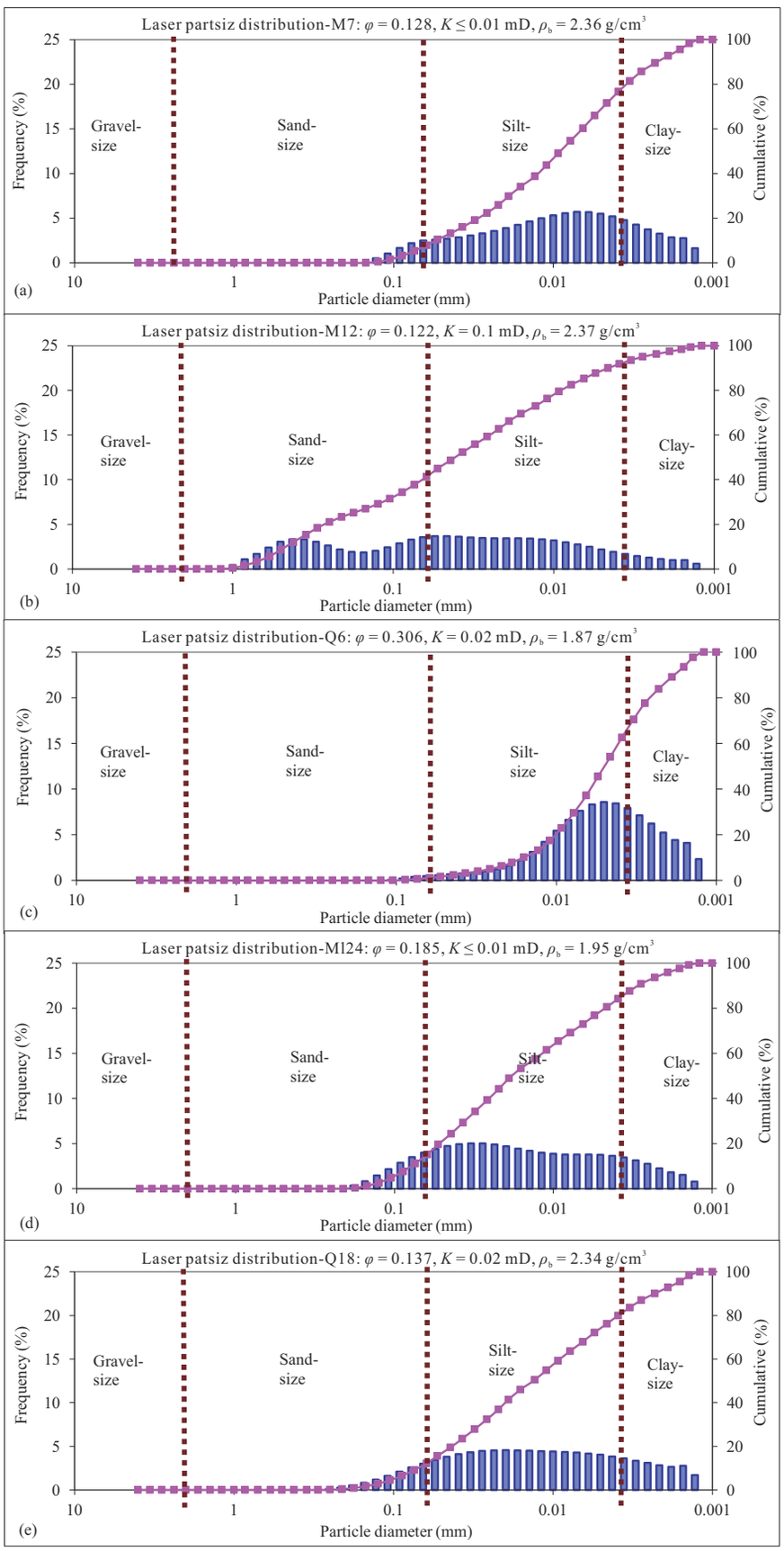

Figure 7. Particle size distribution, frequency distribution, and cumulative frequency curves for five representative samples as obtained by the LPSA (see text for details). The porosity, permeability, and bulk density of each sample are also given.

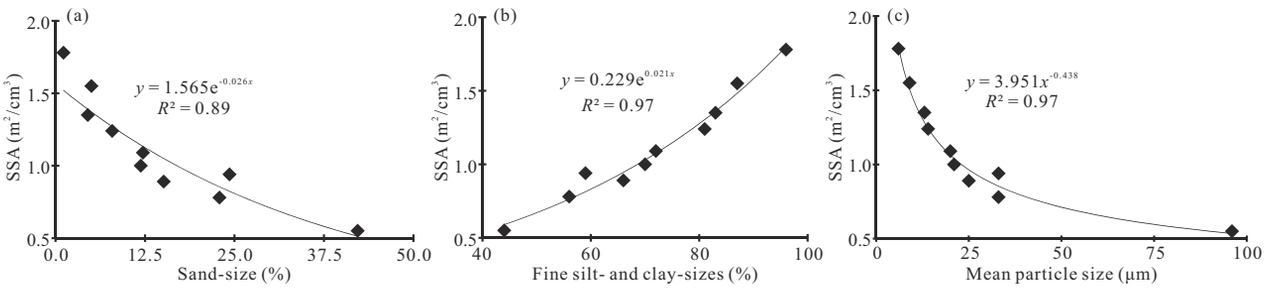

Figure 8. Crossplots between the particle size parameters as obtained by the LPSA. (a) sand-size percentage vs the SSA (m^2/cm^3); (b) the fine silt- and clay-sizes (percentage) vs SSA; and (c) the mean particle size vs SSA.

er hand, samples M3 and M12 are dominated by medium-to coarse-size pores with a small quantity of micropores (Figs. 3g–3h).

Values of the FZI are used by many researchers as a tool for ranking the quality of the rocks as potential reservoirs (Amaefule et al., 1993). In general, rocks containing high proportions of fine components and poorly sorted rocks tend to have high tortuosity and high surface area, and hence low FZI. On the other hand, coarse-grained well-sorted rocks have low surface area and low tortuosity, hence high FZI values (e. g., Kassab et al., 2016). The obtained FZI values for 6 samples are very low and range from 0.03 to 0.28 μm. Although the average porosity of the studied samples is high (0.21), both permeability and the FZI values are very low, which point to a corresponding impermeable reservoir based on the distinction of Nabawy and Al-Azazi (2015) and Nabawy et al. (2018).

4.2 Pore Throat Size Characterization Based on MICP Data

Based on the obtained curves in Fig. 6a, three types of pore throat sizes can be characterized: Type I (samples M3, M12, Q15, and Q18), Type II (samples M7, M16, Q1, and Q6), and Type III (samples Ml21 and Ml24). Some segments of the saturation curves of a few samples are flat (e.g., samples Ml21, Ml24, Q15, and Q18; Fig. 6a), while other samples (M3, M12, and M16) have steeper plateaus, indicating different sorting of the pore throat sizes (Vavra et al., 1992). Steep curve gradients also indicate that large pores in the rock are connected by small throats (Wardlaw and McKellar, 1981). The injection curves end with rising tails of different steepnesses due to the gradual filling of the small toroidal spaces at the boundaries of pores (Fig. 6a). The observed different entry pressures have a direct relationship with the pore throat size distribution of the respective samples (e.g., Medina et al., 2018). According to Wardlaw and McKellar (1981), the P_{th} is also affected by the coordination number (the average number of throats connected to each pore) and the arrangement of the pore system elements (pores + throats). The P_{th} for type I samples is the lowest and varies from 79 to 405 psi (Table 1, Fig. 6a), but from 1 382 to 2 081 psi for type II samples. Samples of type III pore throats, on the other hand, require much higher threshold pressures for mercury injection (Table 1). Petrographic and SEM analyses validate these three categories, where type I samples are composed of medium to coarse, well-connected, micrite crystals of >2 – 5 mm (Figs. 3c, 3g; and Figs. 5a, 5d). Moreover, the contacts between micrite particles in this category are coarse punctic to partially coalescent. Type I samples have, however, moderate/good porosity (12% – 35%) but poor permeability (Table 1). The pore throat radii of these samples are larger than those of the other two types (Fig. 6b). Moreover, the relatively lower P_{th} of samples Q15 and Q18 and the gentle slope of the central part of the intrusion curves point to the ease with which mercury intrudes the pore system due to higher degrees of pore interconnectivity. Type II samples are composed of fine (<2.5 mm) micrite particles (Figs. 3e, and 3f), and small pore throat radii of <1 mm (Fig. 6b). However, the contacts between the micrite particles are fine punctic to partially coalescent. The morphology of micrite particles in this type is subrounded to fitted bounding subhedral. Permeability of these samples is also very low, even though porosity is moderate to high (Table 1). Janjuhah et al. (2018) reported that due to the development of isolated micropores, permeability is very low. Type III samples are mainly composed of fitted bounding subhedral and fitted fused anhedral micrite textures (Figs. 3d and 5b). Diagenesis strongly impacted these samples, forming dense micrite particles that destroy porosity and permeability. As discussed earlier, different types of microporosity in rocks in southern Lebanon might involve different mechanisms in the development of micrite crystallometry and microporosity. In many shallow marine carbonate deposits, marine diagenesis is a very common diagenetic process (Wilson, 2002; Munnecke et al., 2008). In that case, compaction is the major contributor where most bioclasts are broken down due to overburden pressure (Figs. 5h, 5i, 5j), and the porosity is destroyed, creating more space for micrite envelops. The micrite envelops, micritized grains, and matrix are very common in the studied samples and form an important portion of the micropore network (Figs. 5e–5j). Partial to complete micritization of grains is significantly observed in studied samples (Figs. 5e–5j). Moreover, the process of cementation is the major cause of the development of microporosity in fine to medium-crystalline cement (Figs. 3c, 3f, 3g, and 5b). During the process of crystal growth, the water precipitates some components at the crystal interface, resulting in a microporous cement (Cantrell and Hagerty, 1999). Al-Aasm and Azmy (1996), Cantrell and Hagerty (1999), Pittman (1971), and Lucia and Loucks (2013), pointed out that all the diagenetic alterations of carbonate rocks occur mostly in the presence of water, but intercrystalline micropores survive the diagenetic alteration. These micropores are also observed, although not dominant. On average, 90% of the documented micropores in this class

are isolated in nature, or connected by very low pore throat radii (Fig. 6b).

Curve similarity is poor among Type I and Type II samples, but excellent for the two samples of Type III pore throats (Fig. 6). The poor curve similarity of types I and II pores reflects differences in the pore type, shape, pore throat radius, uniformity of pore throat distribution, and degree of detour (Thomeer, 1960; Luo, 1989). The mean hydraulic radius of the studied representative samples is positively correlated with permeability (Fig. 9a), even though with a fair correlation (R^2 = 0.67). The critical pore throat diameter (D_c) describes the pore spaces of a sample and characterization of the connected pore space with only one parameter (e. g., Norbisrath et al., 2015). The pore throat diameter at a critical pressure is measured when mercury first spans and percolates into a sample (Katz and Thompson, 1985). The D_c can be determined from the curves of mercury saturation versus the pore throat size distribution (Fig. 6b) at the inflection point of the rapidly-rising cumulative mercury saturation (Swanson, 1985; Urai et al., 2008). The obtained D_c values are generally small, ranging from 0.006 to 0.61 µm, and are positively correlated with permeability (R^2 = 0.71, Fig. 9b). Such small values indicate that the pore network of the studied samples is interconnected with small pore throats (Norbisrath et al., 2015). The capillary pressure is linked to the pore aperture through which mercury may penetrate (Dürrast and Siegesmund, 1999). The entry points observed for the tested samples start at different pore throat sizes, which vary from 1.37 µm in sample M3 to low values of only 0.012 µm in sample Ml21 (Fig. 6b). The entry point for sample M12 is 1.2 µm since it contains 17% mesoports. These results illustrate the dominance of micropores and microports in the tested samples. The uniformity of pore size distribution differs among the samples where it varies over broad ranges for the Magdoucheh (M3, M12, and M16) samples, but within narrow ranges for the Qennarit and Choualiq samples. Because the P_{th} value is characteristic of the largest pores, it is inversely related to permeability (Fig. 9c). Higher entry pressures were necessary to inject mercury into the very low-permeability Ml21 and Ml24 samples. This relationship indicates that fluid flow in rocks is supported by the large interconnected pores which are saturated at low entry pressures (Medina et al., 2018). The relationship between porosity and mercury entry pressure is, however, less clear, although there is also a general inverse trend (Fig. 9d).

The incremental pore throat radii distributions are shown in Fig. 10. All samples display only one peak, indicating the dominance of a specific pore throat radius in a given sample. The pore throat sizes of samples Ml21 and Ml24 are very small and very close to each other; thus, they overlap. Although sample Ml21 has a higher porosity than Q18, its permeability is much smaller. They have as much as 18.95% and 19.1% pore throat sizes of 0.003 and 0.177 µm, respectively. In total, six

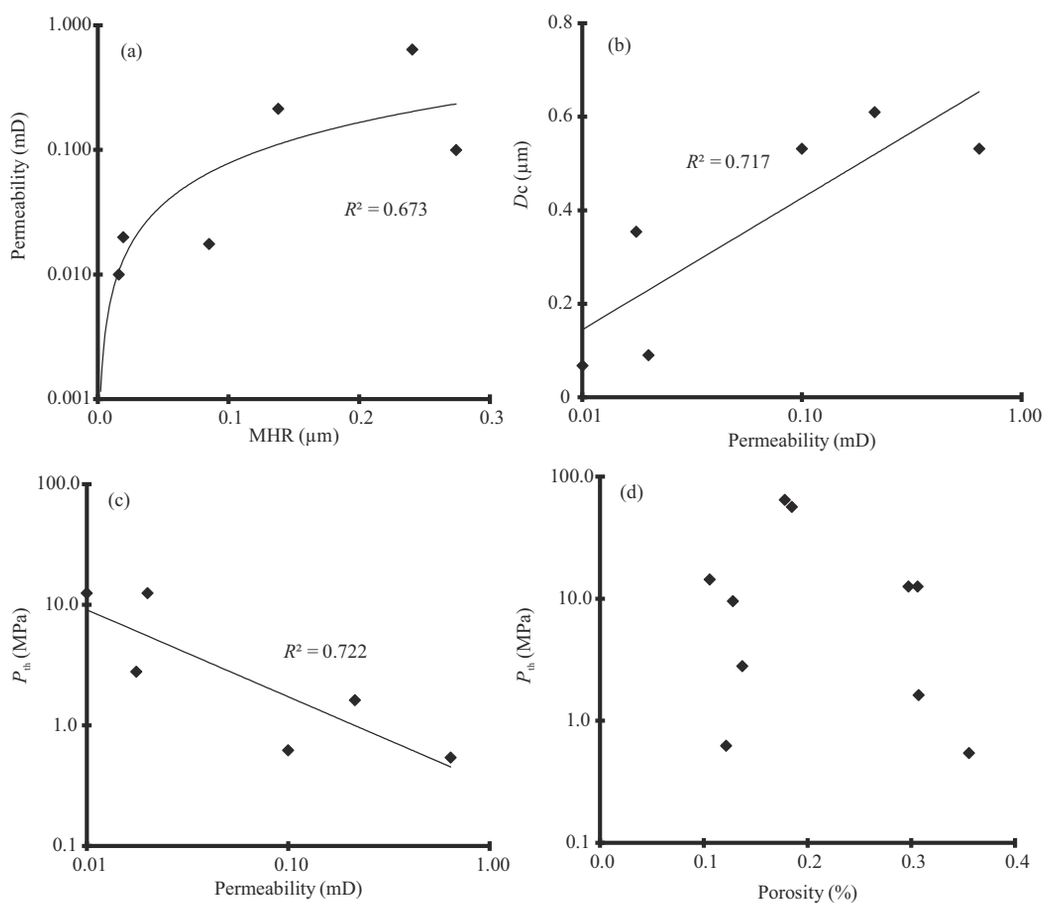

Figure 9. Crossplots between the poro-perm data and the MICP-derived parameters. (a) MHR vs permeability; (b) permeability vs the critical pore size diameter; (c) permeability vs the mercury entry (threshold) pressure (P_{th}); and D) porosity vs P_{th}.

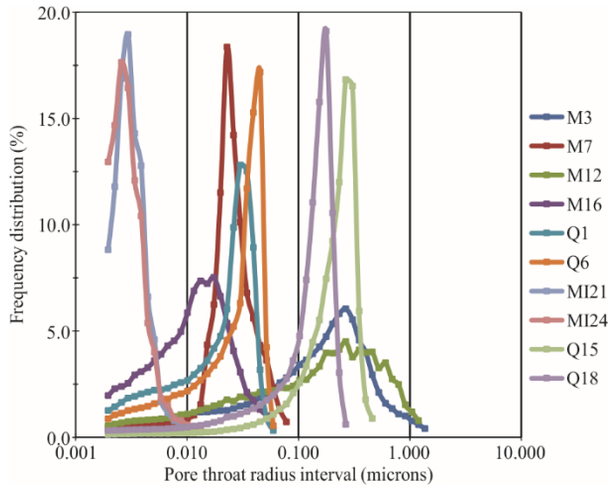

Figure 10. Frequency distributions of the pore throat radii intervals for the studied samples.

Table 3 Pore throat radii in microns at discrete mercury saturations

Pore throat radius	Type I samples	Type II samples	Type III samples
R_{16}	0.20–0.50	0.02–0.05	0.004–0.005
R_{35}	0.16–0.30	0.016–0.040	0.003–0.004
R_{50}	0.14–0.24	0.013–0.033	~0.003
R_{84}	0.02–0.12	0.004–0.02	0.002–0.003
R_{90}	0.01–0.10	0.003–0.015	0.002–0.0025

samples have more than 15% pore throats of a particular size, with the remaining four samples having more homogenous pore throat size distributions. Sample Q1 has a 12.5% pore throat with a size of 0.03 µm. Overall, the investigated samples display three different peaks centred at pore sizes of 0.25, 0.035, and 0.002 µm, which correspond to the three categories of type I, type II, and type III samples. In this way, the MICP technique enabled us to investigate pores with sizes varying over three orders of magnitude from 0.001 to more than 1.0 µm (Figs. 6b, 10), including those that are unresolvable using the thin-section analysis because of the lower resolution.

The MICP results provide valuable information on the pore size distribution, the permeability of the studied samples, and the pore size range in which mercury flows (Fig. 11). The curves of the PSDF are unimodal and leptokurtic, indicating a uniform distribution of pore sizes and generally well-sorted pore throat sizes (Fig. 11a). Pore throat radii at different mercury saturations (16%, 35%, 50%, 84%, and 90%) for the three sample categories are shown in Table 3. It is clear that the fluid flow occurs mainly in the mesoports (detected only in two samples) and the large microports (>0.1 µm). Little fluid flow occurs through micropore throats of less than 0.1 µm in type I samples (Fig. 11b). In Type II samples, the fluid flow occurs within pore throat sizes ranging from 0.01 to 0.1 µm, and in sizes between 0.002 and 0.015 µm in Type III samples.

Although a direct trend is observed between porosity and MHR, there is a considerable scatter where some samples deviate noticeably from the positive trend (Fig. 12a). Based on the petrographic analysis, samples Q1, Q6, Ml21, and Ml24 are

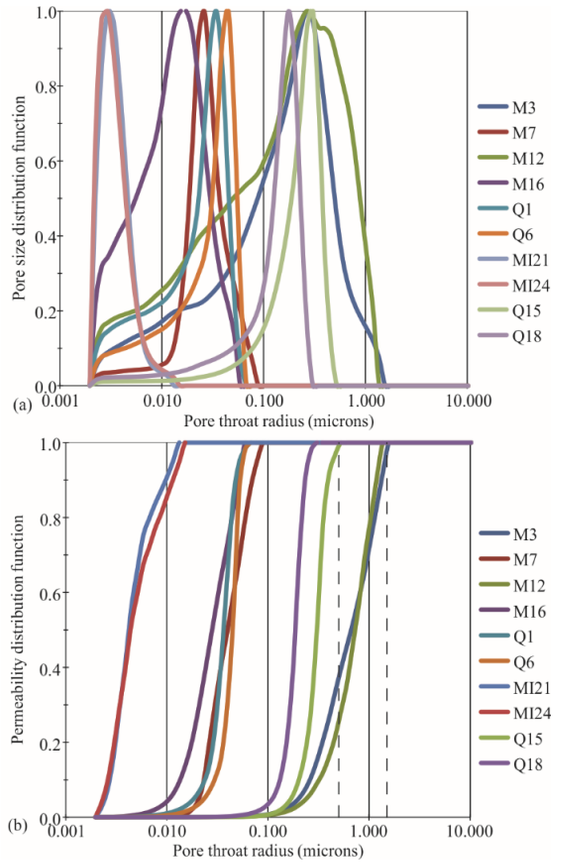

Figure 11. Pore size and permeability distribution functions with respect to the pore throat radii of the investigated samples.

wackestone facies (mud-dominated) with small vuggy pores. The poro-perm relationship indicates that these samples have moderate to good porosities but very small MHR and very low permeability (Table 1, and Fig. 4c). Sample M12 (wackestone/packstone) has a moderate porosity of 0.12 but the largest average MHR, perhaps because of its highest sand-size fraction (Table 2). Although with some scatter, porosity is negatively correlated with the P_{th} (Fig. 12b). Samples M7, M12, M16, and Q18 have low to moderate porosities and also low to moderate threshold pressures. The petrographic and SEM investigations of these samples represent a high degree of micritization and cementation (Figs. 3c, and 5a, 5f). The two diagenetic processes have a negative impact on both porosity and permeability because micritization initially destroys the grains, then cementation fills the empty pore spaces and isolates the micropores, thus reducing the porosity and permeability. On the other hand, a strongly inverse correlation exists, on the other hand, between the MHR and the P_{th} (Fig. 12c), allowing the prediction of the pore throat sizes from the entry pressure with great accuracy. Indeed, this is the basis of the MICP technique.

4.3 Permeability and MICP Data

The average permeability of the studied samples is less than 1 mD, which indicates that the investigated samples are nearly impermeable (Table 1). Previous studies revealed that permeability is dependent not only on porosity but also on pore size, pore throat radius, tortuosity, and surface area (e.g., Jaya

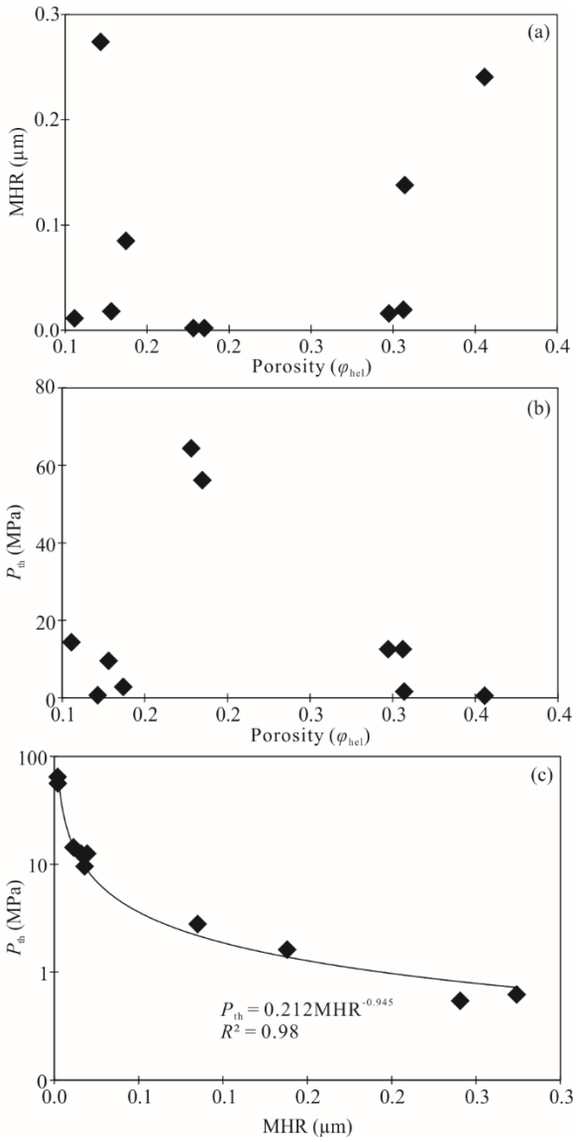

Figure 12. Crossplots showing the relationships between porosity and other MICP-derived parameters. (a) Porosity vs MHR; (b) porosity vs P_{th}; and (c) MHR vs P_{th}.

et al., 2005). Rushing et al. (2008) demonstrated that permeability is affected more strongly by the ratio of the pore/pore throat radii than by porosity itself. Additionally, the presence of fine-grained components in a sample blocks the connectivity of the pores, which impacts permeability adversely. All of the studied representative samples have clay-sized particles with ratios varying from 8.1% to 37.5% and an average of 21.29% (Table 2). The average shale-size fraction in the studied rocks is also very high (71.5%). On the other hand, the studied samples have dominantly very small micropore throats, with only two samples having a small amount of mesoports. Such small pore throat radii need very high pressures for mercury injection (Table 1). The obtained MHR values are also very small. The results obtained by the MICP pore throat characterization and the grain size data from LPSA, therefore, support the observed very low permeability of the studied samples.

Unlike sandstones, the pore spaces in carbonate rocks have complicated geometry due to the presence of various components such as shells and carbonate grains (Clark and Kleinberg, 2002). Moreover, the diagenetic processes modify carbonate rock properties, complicating the prediction of their permeability (Westphal et al., 2005). Conventional reservoirs exhibit good poro-perm relationships in contrast to unconventional reservoirs that display poor poro-perm relationships due to the presence of narrow pore throat radii or pore structures (e. g., Nelson, 1994; Ehrenberg and Nadeau, 2005; Zou et al., 2012; Wu et al., 2014).

Mao et al. (2013) investigated the relationship between the Swanson parameter and the pore structure index $(K/\varphi)^{1/2}$, for tight gas sands and found R^2 values of more than 0.96. The high coefficient of determination reveals that this procedure is convenient for estimating permeability once the rock porosity and the Swanson parameter are obtained. Our studied carbonate samples display a positive correlation between the two parameters, although with a considerable scatter and a slightly lower coefficient of correlation (R^2 = 0.88, Fig. 13a). Using the resulting equation between the pore structure index, the helium porosity, and the Swanson parameter, the computed permeability ranges from 0.01 to 0.67 mD with an average of 0.176 mD, which is very close to the average of 0.167 mD of the measured permeability. This means that permeability could be computed from MICP data, especially when a large number of samples are analyzed. Some samples plot below the regression line while others plot above. Samples M12 and Q18 possess almost the same value of the Swanson parameter but different pore structure indices; the same phenomenon is also observed for samples M3 and Q15 (Fig. 13a). The SEM analysis of M12 and M3 indicates that these samples contain medium to coarser micrite particles with a pore size ranging from 4-8 μm (Figs. 3g and 3h), while Q15 and Q18 have very fine to fine micrite microtextures with dominantly fine micropores of less than 2 μm in size (Figs. 3b and 5a, 5d, and 5e). The pore throat radius corresponding to 35% mercury saturation (R_{35}) is also closely related to permeability (Lafage, 2008). The crossplot between R_{35} and the pore structure index (Fig. 13b) displays a positive correlation with a high coefficient of correlation (R^2 = 0.84). Permeability is also positively correlated with the median pore size (Fig. 13c), but with a lower R^2 value of 0.54. A better correlation is, however, found between the threshold pore size (the pore size corresponding to the threshold pressure) and permeability, with a correlation coefficient of 0.72 (Fig. 13d). These fair/moderate coefficients of determination are slightly lower compared to other results, such as those of Basan et al. (1997) for sandstone rocks. The obtained low/moderate R^2 values may also arise from the small number of samples and the widely variable pore throat sizes.

4.4 Reservoir vs Non-Reservoir Rocks

MICP data can be used to distinguish potential reservoir rocks from non-reservoir rocks and, thus, pay *versus* non-pay zones. A reservoir rock is a porous and permeable rock capable of containing hydrocarbons (Sneider, 1987), which has nothing to do with whether a rock actually contains or would produce hydrocarbons. Pay is the hydrocarbon-bearing zone of the reservoir, which will produce at economic rates using a given pro-

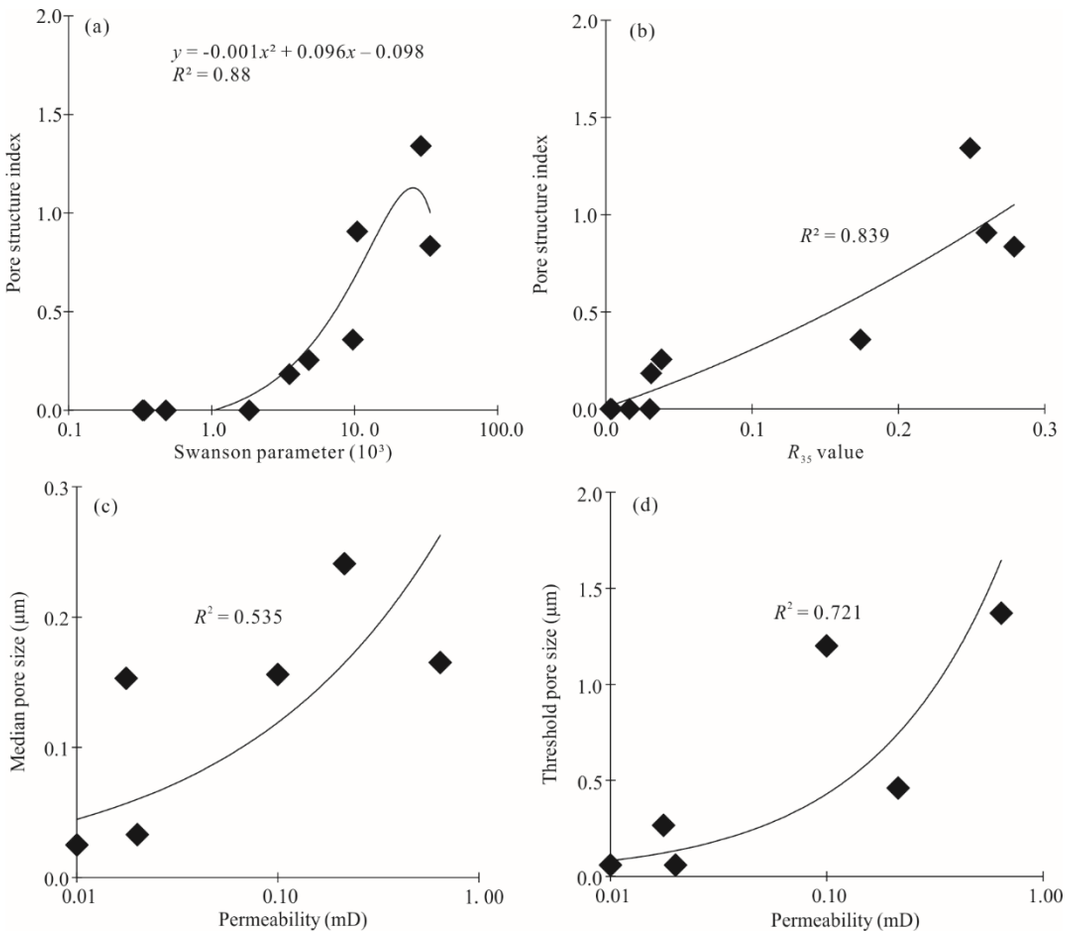

Figure 13. Crossplots between the petrophysical and some MICP-derived parameters. (a) Swanson parameter vs pore structure index; (b) the R_{35} vs pore structure index; (c) permeability vs median pore size; and (d) permeability vs threshold pore size.

duction method. According to Sneider (1987), a reservoir is distinguished from a non-reservoir based on the displacement pressure and the mercury saturation at specific pressures. In a reservoir rock, mercury may occupy 1% of the bulk volume at a pressure of <300 psi, whereas a non-reservoir rock will achieve this saturation at a pressure of >500 psi. At a pressure of 2 000 psi, mercury occupies more than 50% of the pore volume of a reservoir rock but ⩽50% of the pore volume of a non-reservoir rock. According to these criteria, samples of Type I pore throats are distinguished as reservoir rocks, whereas samples of types II and III pore throats are clearly non-reservoir rocks (Fig. 4). However, considering the threshold of displacement pressure (100 psi) as a further criterion, only the two samples, M3 and M12, which contain 10% and 17% mesoports, respectively, could act as reservoir rocks. Additional criteria must be again applied to determine if a reservoir rock is pay or non-pay because not all reservoir rocks are pay.

5 CONCLUSIONS

Several investigations are performed in this study on carbonate rocks collected from Sidon (southern Lebanon) to study the rock pore throat radii, pore and particle sizes, as well as their impact on the petrophysical properties and reservoir characteristics. The obtained results point to heterogeneous fabrics, a diversity of pore throat sizes, high micrite content, and a large amount of micropores. These characteristics are controlled by the depositional environment, composition, subsequent diagenetic processes, and tectonic deformation. Detailed analyses of the MICP and LPSA data accompanied by petrographic and SEM investigations of southern Lebanon carbonate rocks indicate that.

(1) Depositional processes are not the only factors affecting the petrophysical and storage capacity properties of carbonate rocks. Diagenetic processes such as micritization, cementation, dissolution, recrystallization, and dolomitization have a major influence in modifying these properties.

(2) The MICP data revealed the dominance of micropore throat sizes as well as small fractions of mesopore throats only in two samples. Grain sizes vary widely from those of very coarse sand-sizes (~ 2 mm) to the clay-sizes (<0.002 mm). The wide variations both in pore throat radii (spanning 3 orders of magnitude) and particle sizes indicate that the investigated rocks are heterogeneous. The widely-variable pore throat sizes, the absence of macroports, small MHR, and the high P_{th} justify the very low permeability of the tested samples.

(3) Permeability estimation from MICP analysis is challenging in the carbonate rocks of South Lebanon due to the presence of microporosity and a significant amount of silt- and clay-size components.

(4) The small pore throat radii and grain sizes support the

observed low MHR, high entry pressures, and the very low permeability of the studied rocks. Based on the obtained MICP data, few samples among the studied rocks are classified as reservoir rocks.

It is evident that data derived from MICP, along with thin-section petrography and SEM studies, are useful for characterizing and understanding the petrophysical properties of carbonate rocks. Extending the present study to rocks extracted from drilled wells will enable us to characterize the subsurface successions in terms of their storage capacity and reservoir potential.

ACKNOWLEDGMENTS

This research has been supported by a grant from the University Research Board (URB) of the American University of Beirut (AUB) (Nos. 103603, 24687). We are very thankful to Rania Shatila (Central Research Science Laboratory, AUB) and Dr. Alejandro Gallardo (Department of Earth and Ocean Dynamics, University of Barcelona) for their help and technical support during the SEM sessions and thin section preparation. The final publication is available at Springer via https://doi.org/10.1007/s12583-020-1057-8.

REFERENCES CITED

Adamson, A. W., Gast A. P., 1997. Physical Chemistry of Surfaces: 6th Edition. John Wiley & Sons Inc., New York. 120–180

Ahr, W. M., 1989. Early Diagenetic Microporosity in the Cotton Valley Limestone of East Texas. *Sedimentary Geology*, 63(3/4): 275 – 292. https://doi.org/10.1016/0037-0738(89)90136-X

Al-Aasm, I. S., Azmy, K. K., 1996. Diagenesis and Evolution of Microporosity of Middle–Upper Devonian Kee Scarp Reefs, Norman Wells, Northwest Territories, Canada: Petrographic and Chemical Evidence. *AAPG Bulletin*, (1): 82–99. https://doi. org/10.1306/64ed8750-1724-11d7-8645000102c1865d

Al-Gharbi, M. S., Blunt, M. J., 2005. Dynamic Network Modelling of Two-Phase Drainage in Porous Media. *Physical Review E*: *Covering Statistical*, *Nonlinear*, *Biological*, *and Soft Matter Physics*, 71(2): 016308. https://doi.org/10.1103/PhysRevE.71.016308

Al-Kharusi, A. S., Blunt, M. J., 2007. Network Extraction from Sandstone and Carbonate Pore Space Images. *Journal of Petroleum Science and Engineering*, 56(4): 219–231. https://doi.org/10.1016/j.petrol.2006.09.003

Amaefule, J. O., Altunbay, M., Tiab, D., et al., 1993. Enhanced Reservoir Description: Using Core and Log Data to Identify Hydraulic (Flow) Units and Predict Permeability in Uncored Intervals/Wells. In Proceedings of the SPE Annual Technical Conference and Exhibition, October 3 – 6, 1993. Houston, Texas. SPE-26436-MS. https://doi. org/10.2118/26436-MS

Anovitz, L. M., Cole, D. R., 2015. Characterization and Analysis of Porosity and Pore Structures. *Reviews in Mineralogy and Geochemistry*, 80(1): 61–164. https://doi.org/10.2138/rmg.2015.80.04

Anselmetti, F. S., Eberli, G. P., 1999. The Velocity-Deviation Log: A Tool to Predict Pore Type and Permeability Trends in Carbonate Drill Holes from Sonic and Porosity or Density Logs. *AAPG Bulletin*, 83 (3): 450–466. https://doi.org/10.1306/00aa9bce-1730-11d7-8645000102c1865d

Anselmetti, F. S., Eberli, G. P., 1993. Controls on Sonic Velocity in Carbonates. *Pure and Applied Geophysics*, 141(2): 287 – 323. https://doi.org/10.1007/BF00998333

Baechle, G. T., Weger, R., Eberli, G. P., et al., 2004. The Role of Macroporosity and Microporosity in Constraining Uncertainties and in Relating Velocity to Permeability in Carbonate Rocks. Society of Exploration Geophysicists Technical Program Expanded Abstracts 2004. 1662–1665

Bailey, S., 2009. Closure and Compressibility Corrections to Capillary Pressure Data in Shales. Oral Presentation Given at the DWLS 2009 Fall Workshop, beyond the Basics of Capillary Pressure: Advanced Topics and Emerging Applications. Colorado School of Mines, USA

Basan, P. B., Lowden, B. D., Whattler, P. R., et al., 1997. Pore-Size Data in Petrophysics: A Perspective on the Measurement of Pore Geometry. *Geological Society*, *London*, *Special Publications*, 122(1): 47 – 67. https://doi.org/10.1144/gsl.sp.1997.122.01.05

BouDagher-Fadel, M., Clark, G. N., 2006. Stratigraphy, Paleoenvironment and Paleogeography of Maritime Lebanon: A Key to Eastern Mediterranean Cenozoic History. *Stratigraphy*, 3(2): 81–118

Burchette, T. P., 2012. Carbonate Rocks and Petroleum Reservoirs: A Geological Perspective from the Industry. *Geological Society*, *London*, *Special Publications*, 370(1): 17–37. https://doi.org/10.1144/sp370.14

Byrnes, A. P., Cluff, R. M., Webb, J. C., 2009. Analysis of Critical Permeability, Capillary Pressure, and Electrical Properties for Mesaverde Tight Gas Sandstones from Western U. S. Basins. Final Report Submitted by Kansas Geological Survey for United States Department of Energy (DOE) Contract DE-FC26-05NT42660, Accessed January 2010. https://www.kgs.ku.edu/mesaverde/index.html

Cantrell, D. L., Hagerty, R. M., 1999. Microporosity in Arab Formation Carbonates, Saudi Arabia. *GeoArabia*, 4(2): 129–154.

Clark, B., Kleinberg, R, 2002. Physics in Oil Exploration. *Physics Today*, 55 (4): 48–53. https://doi.org/10.1063/1.1480782

Comisky, J. T., Santiago, M., McCollom, B., et al., 2011. Sample Size Effects on the Application of Mercury Injection Capillary Pressure for Determining the Storage Capacity of Tight Gas and Oil Shales. In Proceedings of the Canadian Unconventional Resources Conference, November 15 – 17, 2011. Calgary, Alberta, Canada. SPE-149432-MS. https://doi.org/10.2118/149432-MS

Deville de Periere, M., Durlet, C., Vennin, E., et al., 2011. Morphometry of Micrite Particles in Cretaceous Microporous Limestones of the Middle East: Influence on Reservoir Properties. *Marine and Petroleum Geology*, 28(9): 1727 – 1750. https://doi. org/10.1016/j. marpetgeo.2011.05.002

Dewit, J., Huysmans, M., Muchez, P., et al., 2012. Reservoir Characteristics of Fault-Controlled Hydrothermal Dolomite Bodies: Ramales Platform Case Study. *Geological Society*, *London*, *Special Publications*, 370(1): 83–109. https://doi.org/10.1144/sp370.1

Dillinger, A., Esteban, L., 2014. Experimental Evaluation of Reservoir Quality in Mesozoic Formations of the Perth Basin (Western Australia) by Using a Laboratory Low Field Nuclear Magnetic Resonance. *Marine and Petroleum Geology*, 57(2): 455 – 469. https://doi. org/10.1016/j.marpetgeo.2014.06.010

Dubertret, L., 1945 – 1953. Carte Géologique au 50 000 de la Syrie et du Liban. 21 Sheets and Notes. Damas and Beirut, Ministères de Traveaux Publiques

Dubertret, L., 1955. Carte Géologique du Liban 1 : 200 000. Beirut, Lebanon

Dürrast, H., Siegesmund, S., 1999. Correlation between Rock Fabrics and Physical Properties of Carbonate Reservoir Rocks. *International Journal of Earth Sciences*, 88(3): 392 – 408. https://doi. org/10.1007/s005310050274

Ehrenberg, S. N., Nadeau, P. H., 2005. Sandstone vs Carbonate Petroleum Reservoirs: A Global Perspective on Porosity-Depth and Porosity-Permeability Relationships. *AAPG Bulletin*, 89(4): 435–445. https://doi.org/10.1306/11230404071

Ehrenberg, S. N., Walderhaug, O., 2015. Preferential Calcite Cementation of Macropores in Microporous Limestones. *Journal of Sedimentary Research*, 85(7): 780–793. https://doi.org/10.2110/jsr.2015.52

Folk, R. L., 1959. Practical Petrographic Classification of Limestones. *AAPG Bulletin*, 43(1): 1–38. https://doi.org/10.1306/0bda5c36-16bd-11d7-8645000102c1865d

Gao, Z. Y., Hu, Q. H., 2013. Estimating Permeability Using Median Pore-Throat Radius Obtained from Mercury Intrusion Porosimetry. *Journal of Geophysics and Engineering*, 10(2): 025014. https://doi.org/10.1088/1742-2132/10/2/025014

Gao, Z. Y., Yang, X. B., Hu, C. H., et al., 2019. Characterizing the Pore Structure of Low Permeability Eocene Liushagang Formation Reservoir Rocks from Beibuwan Basin in Northern South China Sea. *Marine and Petroleum Geology*, 99: 107–121. https://doi.org/10.1016/j.marpetgeo.2018.10.005

Hollis, C., Vahrenkamp, V., Tull, S., et al., 2010. Pore System Characterisation in Heterogeneous Carbonates: An Alternative Approach to Widely-Used Rock-Typing Methodologies. *Marine and Petroleum Geology*, 27(4): 772–793. https://doi.org/10.1016/j.marpetgeo.2009.12.002

Hosseini, M., Tavakoli, V., Nazemi, M., 2018. The Effect of Heterogeneity on NMR Derived Capillary Pressure Curves, Case Study of Dariyan Tight Carbonate Reservoir in the Central Persian Gulf. *Journal of Petroleum Science and Engineering*, 171: 1113–1122. https://doi.org/10.1016/j.petrol.2018.08.054

Hu, X. T., Huang, S., 2016. Physical Properties of Reservoir Rocks. Physics of Petroleum Reservoirs. Springer, Berlin, Heidelberg. 7–164. https://doi.org/10.1007/978-3-662-53284-3_2

Janjuhah, H. T., Alansari, A., Gámez Vintaned, J. A., 2019. Quantification of Microporosity and Its Effect on Permeability and Acoustic Velocity in Miocene Carbonates, Central Luconia, Offshore Sarawak, Malaysia. *Journal of Petroleum Science and Engineering*, 175: 108–119. https://doi.org/10.1016/j.petrol.2018.12.035

Janjuhah, H. T., Alansari, A., Ghosh, D. P., et al., 2018. New Approach towards the Classification of Microporosity in Miocene Carbonate Rocks, Central Luconia, Offshore Sarawak, Malaysia. *Journal of Natural Gas Geoscience*, 3(3): 119 – 133. https://doi.org/10.1016/j.jnggs.2018.05.001

Jaya, I., Sudaryanto, A., Widarsono, B., 2005. Permeability Prediction Using Pore Throat and Rock Fabric: A Model from Indonesian Reservoirs. In Proceedings of the SPE Asia Pacific Oil and Gas Conference and Exhibition, April 5–7, 2005. Jakarta, Indonesia. SPE-93363-MS. https://doi.org/10.2118/93363-MS

Jones, S. C., 1972. A Rapid Accurate Unsteady-State Klinkenberg Permeameter. *Society of Petroleum Engineers Journal*, 12(5): 383–397. https://doi.org/10.2118/3535-pa

Kaczmarek, S. E., Fullmer, S. M., Hasiuk, F. J., 2015. A Universal Classification Scheme for the Microcrystals that Host Limestone Microporosity. *Journal of Sedimentary Research*, 85(10): 1197–1212. https://doi.org/10.2110/jsr.2015.79

Kassab, M. A., Abuseda, H. H., El Sayed, N. A., et al., 2016. Petrographical and Petrophysical Integrated Studies, Jurassic Rock Samples, North Sinai, Egypt. *Arabian Journal of Geosciences*, 9(2): 99. https://doi.org/10.1007/s12517-015-2146-3

Katz, A. J., Thompson, A. H., 1985. Fractal Sandstone Pores: Implications for Conductivity and Pore Formation. *Physical Review Letters*, 54(12): 1325–1328. https://doi.org/10.1103/PhysRevLett.54.1325

Klaver, J., Hemes, S., Houben, M., et al., 2015. The Connectivity of Pore Space in Mudstones: Insights from High-Pressure Wood's Metal Injection, BIB-SEM Imaging, and Mercury Intrusion Porosimetry. *Geofluids*, 15(4): 577–591. https://doi.org/10.1111/gfl.12128

Labani, M. M., Rezaee, R., Saeedi, A., et al., 2013. Evaluation of Pore Size Spectrum of Gas Shale Reservoirs Using Low Pressure Nitrogen Adsorption, Gas Expansion and Mercury Porosimetry: A Case Study from the Perth and Canning Basins, Western Australia. *Journal of Petroleum Science and Engineering*, 112: 7–16. https://doi.org/10.1016/j.petrol.2013.11.022

Lafage, S. I., 2008. An Alternative to the Winland R35 Method for Determining Carbonate Reservoir Quality: [Dissertation]. Texas A & M University, Texas. 1–102

Lai, J., Wang, G. W., Chen, M., et al., 2013. Pore Structures Evaluation of Low Permeability Clastic Reservoirs Based on Petrophysical Facies: A Case Study on Chang 8 Reservoir in the Jiyuan Region, Ordos Basin. *Petroleum Exploration and Development*, 40(5): 606–614. https://doi.org/10.1016/S1876-3804(13)60079-8

Lapponi, F., Casini, G., Sharp, I., et al., 2011. From Outcrop to 3D Modelling: A Case Study of a Dolomitized Carbonate Reservoir, Zagros Mountains, Iran. *Petroleum Geoscience*, 17(3): 283–307. https://doi.org/10.1144/1354-079310-040

León y León, C. A., 1998. New Perspectives in Mercury Porosimetry. *Advances in Colloid and Interface Science*, 76/77: 341–372. https://doi.org/10.1016/S0001-8686(98)00052-9

Li, J. Q., Zhang, P. F., Lu, S. F., et al., 2019. Scale-Dependent Nature of Porosity and Pore Size Distribution in Lacustrine Shales: An Investigation by BIB-SEM and X-Ray CT Methods. *Journal of Earth Science*, 30(4): 823–833. https://doi.org/10.1007/s12583-018-0835-z

Lima Neto, I. A., Misságia, R. M., Ceia, M. A., et al., 2015. Evaluation of Carbonate Pore System under Texture Control for Prediction of Microporosity Aspect Ratio and Shear Wave Velocity. *Sedimentary Geology*, 323: 43–65. https://doi.org/10.1016/j.sedgeo.2015.04.011

Liu, J. Y., Qiu, Z. S., Huang, W., et al., 2014. Nano-Pore Structure Characterization of Shales Using Gas Adsorption and Mercury Intrusion Techniques. *Journal of Chemical and Pharmaceutical Research*, 6(4): 850–857.

Lucia, F. J., 1995. Rock-Fabric/Petrophysical Classification of Carbonate Pore Space for Reservoir Characterization. *AAPG Bulletin*, 79(9): 1275–1300. https://doi.org/10.1306/7834d4a4-1721-11d7-8645000102c1865d

Lucia, F. J., Loucks, R. G., 2013. Micropores in Carbonate Mud: Early Development and Petrophysics. *Gulf Coast Association of Geological Socities*, 2: 1–10

Luo, M. G., 1989. A Study of the Capillary Curve of the Thick Conglomeratic Reservoir in the 8th Block, Karamay Oil Field, Xinjiang, by $X^2(n)$ Distribution and Its Geological Significance. *Petroleum Expoloration and Development*, 16(1): 73–83 (in Chinese with English Abstract)

Mao, Z. Q., Xiao, L., Wang, Z. N., et al., 2013. Estimation of Permeability by Integrating Nuclear Magnetic Resonance (NMR) Logs with Mercury Injection Capillary Pressure (MICP) Data in Tight Gas Sands. *Applied Magnetic Resonance*, 44(4): 449–468. https://doi.org/10.1007/s00723-012-0384-z

Marschall, D., Gardner, J. S., Mardon, D., et al., 1995. Method for

Correlating NMR Relaxometry and Mercury Injection Data. Paper SCA1995-11, Proc. Int. Symp. Soc. Core Analysts, San Francisco, California, USA, 9511: 40

Mavko, G., Mukerji, T., Dvorkin, J., 2009. The Rock Physics Handbook: Tools for Seismic Analysis of Porous Media. Cambridge University Press, Cambridge

Medina, C. R., Mastalerz, M., Rupp, J. A., 2017. Characterization of Porosity and Pore-Size Distribution Using Multiple Analytical Tools: Implications for Carbonate Reservoir Characterization in Geologic Storage of CO_2. *Environmental Geosciences*, 24(1): 51–72. https://doi.org/10.1306/eg.02071716010

Medina, C. R., Mastalerz, M., Rupp, J. A., 2018. Pore System Characterization of Cambrian-Ordovician Carbonates Using a New Mercury Porosimetry-Based Petrofacies Classification System: Application to Carbon Sequestration Reservoirs. *Greenhouse Gases*: *Science and Technology*, 8(5): 932 – 953. https://doi.org/10.1002/ghg.1806

Michels, K. H., 2000. Inferring Maximum Geostrophic Current Velocities in the Norwegian-Greenland Sea from Settling-Velocity Measurements of Sediment Surface Samples: Methods, Application, and Results. *Journal of Sedimentary Research*, 70(5): 1036 – 1050. https://doi. org/10.1306/101599701036

Morriss, C., Macinnis, J., Freedman, R., et al., 1993. Field Test of an Experimental Pulsed Nuclear Magnetism Tool. SPWLA 34th Annual Logging Symposium June 13 – 16, Calgary, Alberta, Canada, https://onepetro.org/SPWLAALS/proceedings-abstract/SPWLA-1993

Moshier, S. O., 1989. Development of Microporosity in a Micritic Limestone Reservoir, Lower Cretaceous, Middle East. *Sedimentary Geology*, 63(3/4): 217 – 240. https://doi.org/10.1016/0037-0738(89)90133-4

Müller, C., Higazi, F., Hamdan, W., et al., 2010. Revised Stratigraphy of the Upper Cretaceous and Cenozoic Series of Lebanon Based on Nannofossils. *Geological Society*, *London*, *Special Publications*, 341 (1): 287–303. https://doi.org/10.1144/sp341.14

Müller-Huber, E., Börner, F., Börner, J. H., et al., 2018. Combined Interpretation of NMR, MICP, and SIP Measurements on Mud-Dominated and Grain-Dominated Carbonate Rocks. *Journal of Applied Geophysics*, 159: 228–240. https://doi.org/10.1016/j.jappgeo.2018.08.011

Munnecke, A., Westphal, H., Reijmer, J. J. G., et al., 2008. Microspar Development during Early Marine Burial Diagenesis: A Comparison of Pliocene Carbonates from the Bahamas with Silurian Limestones from Gotland (Sweden). *Sedimentology*, 44(6): 977 – 990. https://doi.org/10.1111/j.1365-3091.1997.tb02173.x

Nabawy, B. S., Al-Azazi, N. A. S. A, 2015. Reservoir Zonation and Discrimination Using the Routine Core Analyses Data: The Upper Jurassic Sab'atayn Sandstones as a Case Study, Sab'atayn Basin, Yemen. *Arabian Journal of Geosciences*, 8(8): 5511 – 5530. https://doi.org/10.1007/s12517-014-1632-3

Nabawy, B. S., Barakat, M. K., 2017. Formation Evaluation Using Conventional and Special Core Analyses: Belayim Formation as a Case Study, Gulf of Suez, Egypt. *Arabian Journal of Geosciences*, 10 (2): 25. https://doi.org/10.1007/s12517-016-2796-9

Nabawy, B. S., Rashed, M. A., Mansour, A. S., et al., 2018. Petrophysical and Microfacies Analysis as a Tool for Reservoir Rock Typing and Modeling: Rudeis Formation, Off-Shore October Oil Field, Sinai. *Marine and Petroleum Geology*, 97: 260–276. https://doi.org/10.1016/j.marpetgeo.2018.07.011

Nelson, P. H., 1994. Permeability-Porosity Relationships in Sedimentary Rocks. *Log Analyst*, 35(3): 38–62.

Netto, A. S. T., 1993. Pore-Size Distribution in Sandstones: Geologic Note. *AAPG Bulletin*, 77(6): 1101 – 1104. https://doi. org/10.1306/bdff8df8-1718-11d7-8645000102c1865d

Nooruddin, H. A., Hossain, M. E., Al-Yousef, H., et al., 2014. Comparison of Permeability Models Using Mercury Injection Capillary Pressure Data on Carbonate Rock Samples. *Journal of Petroleum Science and Engineering*, 121: 9–22. https://doi.org/10.1016/j.petrol.2014.06.032

Norbisrath, J. H., Eberli, G. P., Laurich, B., et al., 2015. Electrical and Fluid Flow Properties of Carbonate Microporosity Types from Multiscale Digital Image Analysis and Mercury Injection. *AAPG Bulletin*, 99(11): 2077–2098. https://doi.org/10.1306/07061514205

Nurmi, R., Standen, E., 1997. Carbonates: The Inside Story. *Middle East Well Evaluation Review*, 18: 28–41

Pentecost, A., 2005. Travertine. Springer Nature, Berlin, Heidelberg

Pittman, E. D., 1971. Microporosity in Carbonate Rocks: Geological Notes. *AAPG Bulletin*, 55: 1873 – 1878. https://doi.org/10.1306/819a3db2-16c5-11d7-8645000102c1865d

Purcell, W. R., 1949. Capillary Pressures—Their Measurement Using Mercury and the Calculation of Permeability Therefrom. *Journal of Petroleum Technology*, 1(2): 39–48. https://doi.org/10.2118/949039-g

Rea, D. K., Hovan, S. A., 1995. Grain Size Distribution and Depositional Processes of the Mineral Component of Abyssal Sediments: Lessons from the North Pacific. *Paleoceanography*, 10(2): 251–258.

Rezaee, R., Saeedi, A., Clennell, B., 2012. Tight Gas Sands Permeability Estimation from Mercury Injection Capillary Pressure and Nuclear Magnetic Resonance Data. *Journal of Petroleum Science and Engineering*, 88/89: 92–99. https://doi.org/10.1016/j.petrol.2011.12.014

Rushing, J. A., Newsham, K. E., Blasingame, T. A., 2008. Rock Typing—Keys to Understanding Productivity in Tight Gas Sands. In Proceedings of the SPE Unconventional Reservoirs Conference, February 10 – 12, 2008. Keystone, Colorado, USA. SPE-114164-MS. https://doi.org/10.2118/114164-MS

Salah, M. K., Abd El-Aal, A. K., Abdel-Hameed, A. T., 2019. Influence of Depositional and Diagenetic Processes on the Petrophysical and Mechanical Properties of Lower Miocene Sandstones, Qattara Depression, Northwestern Egypt. *Journal of Petroleum Science and Engineering*, 177: 1114–1133. https://doi.org/10.1016/j.petrol.2019.02.058

Salah, M. K., Alqudah, M., Abd El-Aal, A. K., et al., 2018. Effects of Porosity and Composition on Seismic Wave Velocities and Elastic Moduli of Lower Cretaceous Rocks, Central Lebanon. *Acta Geophysica*, 66(5): 867–894. https://doi.org/10.1007/s11600-018-0187-1

Salah, M. K., Alqudah, M., Monzer, A. J., et al., 2020. Petrophysical and Acoustic Characteristics of Jurassic and Cretaceous Rocks from Central Lebanon. *Carbonates and Evaporites*, 35(1): 12. https://doi.org/10.1007/s13146-019-00536-w

Salah, M. K., El Ghandour, M. M., Abdel-Hameed, A. T., 2016. Effect of Diagenesis on the Petrophysical Properties of the Miocene Rocks at the Qattara Depression, North Western Desert, Egypt. *Arabian Journal of Geosciences*, 9: 329. https://doi.org/10.1007/s12517-015-2275-8

Schlömer, S., Krooss, B. M., 1997. Experimental Characterisation of the Hydrocarbon Sealing Efficiency of Cap Rocks. *Marine and Petroleum Geology*, 14(5): 565 – 580. https://doi. org/10.1016/S0264-8172(97)00022-6

Schmitt, M., Fernandes, C. P., da Cunha Neto, J. A. B., et al., 2013. Characterization of Pore Systems in Seal Rocks Using Nitrogen Gas Adsorption Combined with Mercury Injection Capillary Pressure

Techniques. *Marine and Petroleum Geology*, 39(1): 138–149. https://doi.org/10.1016/j.marpetgeo.2012.09.001

Schön, J. H., 2015. Physical Properties of Rocks—Fundamentals and Principles of Petrophysics: 2nd Edition. Elsevier, Amsterdam

Shanley, K. W., Cluff, R. M., 2015. The Evolution of Pore-Scale Fluid-Saturation in Low-Permeability Sandstone Reservoirs. *AAPG Bulletin*, 99(10): 1957–1990. https://doi.org/10.1306/03041411168

Sigal, R. F., 2009. A Methodology for Blank and Conformance Corrections for High Pressure Mercury Porosimetry. *Measurement Science and Technology*, 20(4): 045108. https://doi. org/10.1088/0957-0233/20/4/045108

Skalinski, M., Kenter, J., 2013. Pore Typing Workflow for Complex Carbonate Systems. AAPG Annual Convention and Exhibition, Pittsburgh, Pennsylvania

Sneider, R. M., 1987. Practical Petrophysics for Exploration and Development. AAPG Education Department Short Course Notes, Variously Paginated

Soete, J., Kleipool, L. M., Claes, H., et al., 2015. Acoustic Properties in Travertines and Their Relation to Porosity and Pore Types. *Marine and Petroleum Geology*, 59: 320–335. https://doi.org/10.1016/j.marpetgeo.2014.09.004

Sun, P. K., Xu, H. M., Dou, Q. F., et al., 2015. Investigation of Pore-Type Heterogeneity and Its Inherent Genetic Mechanisms in Deeply Buried Carbonate Reservoirs Based on Some Analytical Methods of Rock Physics. *Journal of Natural Gas Science and Engineering*, 27: 385–398. https://doi.org/10.1016/j.jngse.2015.08.073

Swanson, B. F., 1981. A Simple Correlation between Permeabilities and Mercury Capillary Pressures. *Journal of Petroleum Technology*, 33 (12): 2498–2504. https://doi.org/10.2118/8234-pa

Swanson, B. F., 1985. Microporosity in Reservoir Rocks: Its Measurement and Influence on Electrical Resistivity. *The Log Analyst*, 26: 42–52

Theologou, P. N., Skalinski, M., Mallan, R. K., 2015. An MICP-Based Pore Typing Workflow—Core Scale to Log Scale. SPWLA 56th Annual Logging Symposium

Thomeer, J. H. M., 1960. Introduction of a Pore Geometrical Factor Defined by the Capillary Pressure Curve. *Journal of Petroleum Technology*, 12(3): 73–77. https://doi.org/10.2118/1324-g

Trentesaux, A., Recourt, P., Bout-Roumazeilles, V., et al., 2001. Carbonate Grain-Size Distribution in Hemipelagic Sediments from a Laser Particle Sizer. *Journal of Sedimentary Research*, 71(5): 858–862. https://doi.org/10.1306/2dc4096e-0e47-11d7-8643000102c1865d

Urai, J., Nover, G., Zwach, C., et al., 2008. Transport Processes. In: Littke, R., Bayer, U., Gajewski, D., et al., eds., Dynamics of Complex Intracontinental Basins: The Central European Basin System. Springer-Verlag, Berlin. 367–388

Vavra, C. L., Kaldi, J. G., Sneider, R. M., 1992. Geological Applications of Capillary Pressure: A Review (1). *AAPG Bulletin*, 76(6): 840–850. https://doi.org/10.1306/bdff88f8-1718-11d7-8645000102c1865d

Walley, C. D., 1997. The Lithostratigraphy of Lebanon: A Review. *Lebanese Science Bulletin*, 10: 81–108

Walley, C. D., 1998. Some Outstanding Issues in the Geology of Lebanon and Their Importance in the Tectonic Evolution of the Levantine Region. *Tectonophysics*, 298(1/2/3): 37–62. https://doi. org/10.1016/S0040-1951(98)00177-2

Wang, P. F., Jiang, Z. X., Yin, L. S., et al., 2017. Lithofacies Classification and Its Effect on Pore Structure of the Cambrian Marine Shale in the Upper Yangtze Platform, South China: Evidence from FE-SEM and Gas Adsorption Analysis. *Journal of Petroleum Science and Engineering*, 156: 307–321. https://doi.org/10.1016/j.petrol.2017.06.011

Wang, X. D., Yang, S. C., Zhao, Y. F., et al., 2018. Improved Pore Structure Prediction Based on MICP with a Data Mining and Machine Learning System Approach in Mesozoic Strata of Gaoqing Field, Jiyang Depression. *Journal of Petroleum Science and Engineering*, 171: 362–393. https://doi.org/10.1016/j.petrol.2018.07.057

Wardlaw, N. C., 1976. Pore Geometry of Carbonate Rocks as Revealed by Pore Casts and Capillary Pressure. *AAPG Bulletin*, 60(2): 245–257. https://doi.org/10.1306/83d922ad-16c7-11d7-8645000102c1865d

Wardlaw, N. C., McKellar, M., 1981. Mercury Porosimetry and the Interpretation of Pore Geometry in Sedimentary Rocks and Artificial Models. *Powder Technology*, 29(1): 127–143. https://doi.org/10.1016/0032-5910(81)85011-5

Washburn, E. W., 1921. The Dynamics of Capillary Flow. *Physical Review*, 17(3): 273–283. https://doi.org/10.1103/physrev.17.273

Westphal, H., Surholt, I., Kiesl, C., et al., 2005. NMR Measurements in Carbonate Rocks: Problems and an Approach to a Solution. *Pure and Applied Geophysics*, 162(3): 549–570. https://doi.org/10.1007/s00024-004-2621-3

Wilson, M. E. J., 2002. Cenozoic Carbonates in Southeast Asia: Implications for Equatorial Carbonate Development. *Sedimentary Geology*, 147(3/4): 295–428. https://doi. org/10.1016/S0037-0738(01)00228-7

Wood, D. A., Hazra, B., 2017. Characterization of Organic-Rich Shales for Petroleum Exploration & Exploitation: A Review-Part 1: Bulk Properties, Multi-Scale Geometry and Gas Adsorption. *Journal of Earth Science*, 28(5): 739–757. https://doi. org/10.1007/s12583-017-0732-x

Wu, Y., Fan, T. L., Zhang, J. C., et al., 2014. Characterization of the Upper Ordovician and Lower Silurian Marine Shale in Northwestern Guizhou Province of the Upper Yangtze Block, South China: Implication for Shale Gas Potential. *Energy & Fuels*, 28(6): 3679–3687. https://doi.org/10.1021/ef5004254

Xu, C. C., Torres-Verdín, C., 2013. Pore System Characterization and Petrophysical Rock Classification Using a Bimodal Gaussian Density Function. *Mathematical Geosciences*, 45(6): 753–771. https://doi.org/10.1007/s11004-013-9473-2

Yu, Y. X., Luo, X. R., Wang, Z. X., et al., 2019. A New Correction Method for Mercury Injection Capillary Pressure (MICP) to Characterize the Pore Structure of Shale. *Journal of Natural Gas Science and Engineering*, 68: 102896. https://doi.org/10.1016/j.jngse.2019.05.009

Zhang, N., He, M. C., Zhang, B., et al., 2016. Pore Structure Characteristics and Permeability of Deep Sedimentary Rocks Determined by Mercury Intrusion Porosimetry. *Journal of Earth Science*, 27(4): 670–676. https://doi.org/10.1007/s12583-016-0662-z

Zou, C. N., Zhu, R. K., Liu, K. Y., et al., 2012. Tight Gas Sandstone Reservoirs in China: Characteristics and Recognition Criteria. *Journal of Petroleum Science and Engineering*, 88/89: 82–91. https://doi.org/10.1016/j.petrol.2012.02.001